Robotica (2012) volume 30, pp. 755–771. © Cambridge University Press 2011
doi:10.1017/S0263574711001007

The coordinated motion planning of a dual-arm space robot for target capturing

Wenfu Xu†, Yu Liu‡* and Yangsheng Xu§

† *Shenzhen Graduate School, Harbin Institute of Technology, Shenzhen 518055, P.R. China*
‡*State Key Laboratory of Robotics and System, Harbin Institute of Technology, Harbin 150001, P.R. China*
§*Department of Automation and Computer-Aided Engineering, The Chinese University of Hong Kong, Hong Kong, P.R. China*

(Accepted August 11, 2011. First published online: September 15, 2011)

SUMMARY
In this paper, autonomous motion control approaches to generate the coordinated motion of a dual-arm space robot for target capturing are presented. Two typical cases are studied: (a) The coordinated dual-arm capturing of a moving target when the base is free-floating; (b) one arm is used for target capturing, and the other for keeping the base fixed inertially. Instead of solving all the variables in a unified differential equation, the solution equation of the first case is simplified into two sub-equations and practical methods are used to solve them. Therefore, the computation loads are largely reduced, and feasible trajectories can be determined. For the second case, we propose to deal with the linear and angular momentums of the system separately. The linear momentum conservation equation is used to design the configuration and the mounted pose of a balance arm to keep the inertial position of the base's center of mass, and the angular momentum conservation equation is used to estimate the desired momentum generated by the reaction wheels for maintaining the inertial attitude of the base. Finally, two typical tasks are simulated. Simulation results verify the corresponding approaches.

KEYWORDS: Dual-arm space robot; Coordinated motion; Target capturing; Path planning.

1. Introduction

Robotic systems are expected to play an increasingly important role in future space activities. One broad area of application is in the servicing, construction, and maintenance of satellites and large space structures in orbit. Therefore, space robotic technologies have been emphasized by many countries.[1–8] The Orbital Express system,[7] sponsored and led by the Defense Advanced Research Projects Agency (DARPA), validated on-orbit satellite servicing technologies. The most remarkable mission was that a satellite autonomously rendezvoused with and captured another satellite in space. Such technologies could lower costs and prolong legacy satellites flying for 5, 10, or even 15 extra years.

* Corresponding author. E-mail: lyu11@hit.edu.cn

The autonomous target-capturing technology, which has been successfully demonstrated by the Engineering Test Satellite VII (ETS-VII)[3] and orbital express,[7] is one of the key technologies of space robot for on-orbit servicing. Unlike on the earth, space operations require the ability to work in unstructured environment.[9] Some autonomous behaviors are necessary to perform complex and difficult tasks in space. This level of autonomy relies not only on vision, force, torque, and tactile sensors but also on advanced planning and control capabilities. Yoshida and Umetani developed on-line control scheme with vision feedback, which used concept of generalized Jacobian matrix (GJM) for motion control and guaranteed workspace (GWS) for path planning.[10,11] McCourt and Silva[12] investigated the use of model-based predictive control for the capture of a multi-Degree of Freedom (DOF) object that moves in a somewhat arbitrary manner. Compared with a single-arm space robot, a dual-arm or multi-arm system has much more dexterity and flexibility, and can complete more complex tasks. Papadopoulos[13] presented a coordinated control scheme for space manipulators and their spacecraft. Moosavian and Papadopoulos[14] developed two basic approaches: the barycentric vector approach and the direct path method to kinematically model multi-arm space free-flying robots, and proposed Multiple Impedance Control (MIC) for manipulating objects with force tracking restrictions.[15] Hu and Vukovich[16] proposed a position and force control method that deals with the control problems of multiple space robots, which form closed kinematic chains. Yoshida *et al.*[17,18] developed some methods to control two arms simultaneously: one arm traces a given path, while the other arm works both to keep the satellite attitude and to optimize a total operation torque of the system. However, much more variables ($n_1 + n_2 + 3$, where n_1, n_2, and 3 are, respectively, for the first arm, the second arm, and the reaction wheels) were required to be solved from a unified kinematic equation. The computation load is large and complex dynamic singularities resulting from the inverse differential kinematic equation may exist.[19] Similarly, Huang *et al.*[20] also designed coordinated control concept to balance the base attitude using the balance arm to counteract the disturbance generated by the mission arm. Agrawal *et al.*[21] presented a scheme for motion planning of a dual-arm, free-floating planar manipulator, where one arm is commanded to perform

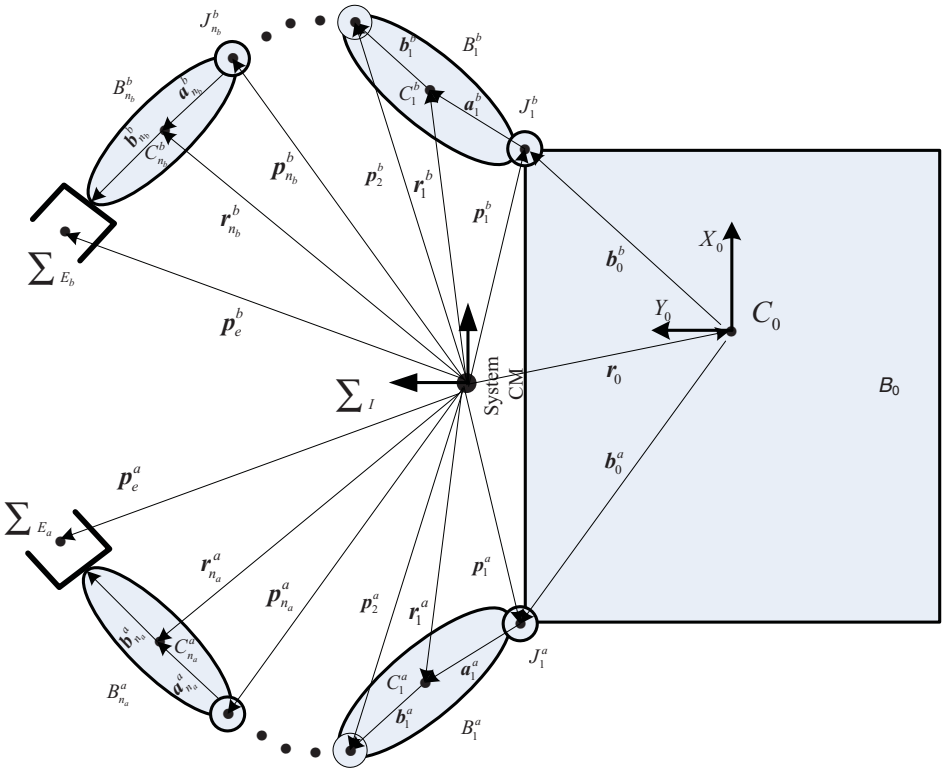

Fig. 1. (Colour online) The general model of a dual-arm space robotic system.

desired tasks whereas the other provides compensating motions to keep the base fixed inertially. They derived the necessary mathematical conditions and implemented some algorithms in joint coordinates and Cartesian coordinates. However, the equation to solve the motion of the balance arm is possibly singular and may not give the feasible results at singularities, especially for complex manipulation.

In this paper, we proposed on-line scheme to control the coordinated motion of a dual-arm space robot for target capturing. Two cases are studied: (a) The coordinated dual-arm capturing of a moving target when the base is free-floating (both the attitude and position are not controlled); (b) one arm is used for target capturing, and the other for keeping the base fixed inertially. Case (a) is partly similar to that of ref. [17] and [18], but the solution equation is simplified into two sub-equations and practical methods are used to solve them. Hence, the computation loads are largely reduced, and feasible trajectories can be determined. For case (b), we addressed a concept to keep the base fixed inertially during capturing. The key of the concept is that the linear and angular momentums of the system are handled separately. The linear momentum conservation equation is used to design the configuration and the mounted pose of the balance arm to keep the inertial position of the base's center of mass (CM). On the other hand, the angular momentum conservation equation is used to estimate the desired momentum generated by the reaction wheels for maintaining the inertial attitude of the base.

The paper is organized as follows: Section 2 derives the kinematic equations of a dual-arm space robotic system. Section 3 presents coordinated motion control methods to generate the trajectories of dual arms to capture a moving target corresponding to two typical cases. In Section 4, simulation studies of the two cases are implemented. Section 5 is the discussion and conclusion of the work.

2. The Motion Equations of a Dual-Arm Space Robot

Major research achievements on space robot were collected by Xu and Kanade.[22] Figure 1 shows a general model of a dual-arm space robotic system, which is composed of the base satellite, a n_a DOFs serial manipulator (arm-a), and a n_b DOFs serial manipulator (arm-b). Symbol B_0 denotes the satellite main body, B_i^a $(i = 1, ..., n_a)$ and B_i^b $(i = 1, ..., n_b)$, respectively, denote the ith link of arm-a and arm-b, and J_i^a and J_i^b are the ith joints of arm-a and arm-b, respectively.

In order to discuss conveniently, some symbols and variables are defined as follows (the following vectors are described in the inertia frame, if not pointed out specially):

$\sum_I$: The inertia frame, whose origin lies at the system's CM.
$\sum_{Ea}, \sum_{Eb}$: The end-effector frames of arm-a and arm-b respectively.
$\sum_B$: The geometry reference of the base, often defined at the center of the payload attach fitting (PAF).
C_i^k $(k = a, b)$: The position of B_i^k's CM.
$\boldsymbol{a}_i^k, \boldsymbol{b}_i^k \in \boldsymbol{R}^3 (k = a, b)$: Position vectors from J_i^k to C_i^k and C_i^k to J_{i+1}^k, respectively, and $\boldsymbol{l}_i^k = \boldsymbol{a}_i^k + \boldsymbol{b}_i^k$.
$\boldsymbol{r}_i^k \in \boldsymbol{R}^3 (k = a, b)$: The position vector of C_i^k.
$\boldsymbol{r}_g \in \boldsymbol{R}^3$: The position vector of the system's CM.
$\boldsymbol{p}_i^k \in \boldsymbol{R}^3 (i = 1, \ldots, n)$: The position vector of J_i^k.
$\boldsymbol{p}_e^k \in \boldsymbol{R}^3 (k = a, b)$: The position vector of the end-effector of arm-k.

https://doi.org/10.1017/S0263574711001007 Published online by Cambridge University Press

$\boldsymbol{k}_i^k \in \boldsymbol{R}^3 (k = a, b)$: The unit vector representing the rotation direction of J_i^k.
$\boldsymbol{\psi}_b, \boldsymbol{\psi}_e \in \boldsymbol{R}^3$: The attitude angle of the base and the end-effector, expressed in terms of z–y–x Euler angles, i.e., $\boldsymbol{\psi}_b = [\alpha_b, \beta_b, \gamma_b]^T$ and $\boldsymbol{\psi}_e = [\alpha_e, \beta_e, \gamma_e]^T$.
${}^i\boldsymbol{A}_j \in \boldsymbol{R}^{3\times 3}$: The rotation matrix of $\sum_j$ with respect to $\sum_i$. When $\sum_i$ is the inertia frame, the superscript i can be missed. The matrix ${}^i\boldsymbol{A}_j$ is described by $[{}^i\boldsymbol{n}_j, {}^i\boldsymbol{o}_j, {}^i\boldsymbol{a}_j]$.
$\dot{\boldsymbol{x}}_b \in \boldsymbol{R}^6$: The linear velocity and angular velocity of B_0.
$\dot{\boldsymbol{x}}_e^k \in \boldsymbol{R}^6 (k = a, b)$: The linear velocity and angular velocity of arm-k's end-effector.
$\boldsymbol{\Theta}^k \in \boldsymbol{R}^{n_k} (k = a, b)$: The actual joint angle vector of arm-k.
$\boldsymbol{\Theta}_d^k \in \boldsymbol{R}^{n_k} (k = a, b)$: The desired joint angle vector of arm-k.
$m_0, m_i^k (k = a, b)$: The mass of B_0 and B_i^k, and total mass of the system is $M = m_0 + \sum_{i=1}^{n_a} m_i^a + \sum_{i=1}^{n_b} m_i^b$.
$\boldsymbol{I}_0, \boldsymbol{I}_i^k \in \boldsymbol{R}^{3\times 3} (k = a, b)$: The inertia matrixes of B_0 and B_i^k with respect to the CM of each body.
$\boldsymbol{E}_3$: 3×3 identity matrix.

From Fig. 1, the position of the end-effector of arm-k $(k = a, b)$ is as follows:

$$\boldsymbol{p}_e^k = \boldsymbol{r}_0 + \boldsymbol{b}_0^k + \sum_{i=1}^{n_k} \left(\boldsymbol{a}_i^k + \boldsymbol{b}_i^k\right), \quad k = a, b. \tag{1}$$

Differentiating it with respect to time, a relationship between the end-effector linear velocity and joint velocity is obtained, i.e.,

$$\boldsymbol{v}_e^k = \dot{\boldsymbol{p}}_e^k = \boldsymbol{v}_0 + \boldsymbol{\omega}_0 \times \left(\boldsymbol{p}_e^k - \boldsymbol{r}_0\right) + \sum_{i=1}^{n_k} \left[\boldsymbol{k}_i^k \times \left(\boldsymbol{p}_e^k - \boldsymbol{p}_i^k\right)\right] \dot{\theta}_i^k, \quad k = a, b. \tag{2}$$

On the other hand, a relationship between the end-effector angular velocity and joint velocity is expressed with

$$\boldsymbol{\omega}_e^k = \boldsymbol{\omega}_0 + \sum_{i=1}^{n_k} \boldsymbol{k}_i^k \dot{\theta}_i^k, \quad k = a, b. \tag{3}$$

Then the differential kinematic equation can be determined according to Eqs. (2) and (3), i.e.,

$$\dot{\boldsymbol{x}}_e^k = \begin{bmatrix} \boldsymbol{v}_e^k \\ \boldsymbol{\omega}_e^k \end{bmatrix} = \boldsymbol{J}_b^k \begin{bmatrix} \boldsymbol{v}_0 \\ \boldsymbol{\omega}_0 \end{bmatrix} + \boldsymbol{J}_m^k \dot{\boldsymbol{\Theta}}^k, \quad k = a, b, \tag{4}$$

where $\boldsymbol{J}_b$ and $\boldsymbol{J}_m$ are the Jacobian matrixes dependent on the base and the manipulator, respectively.

$$\boldsymbol{J}_b^k = \begin{pmatrix} \boldsymbol{E}_3 & -\tilde{\boldsymbol{p}}_{0e}^k \\ \boldsymbol{O} & \boldsymbol{E}_3 \end{pmatrix} \in \boldsymbol{R}^{6\times 6}, \quad \boldsymbol{p}_{0e}^k = \boldsymbol{p}_e^k - \boldsymbol{r}_0, \quad k = a, b, \tag{5}$$

$$\boldsymbol{J}_m^k = \begin{bmatrix} \boldsymbol{k}_1^k \times \left(\boldsymbol{p}_e^k - \boldsymbol{p}_1^k\right) & \cdots & \boldsymbol{k}_n^k \times \left(\boldsymbol{p}_e^k - \boldsymbol{p}_n^k\right) \\ \boldsymbol{k}_1^k & \cdots & \boldsymbol{k}_n^k \end{bmatrix} \in \boldsymbol{R}^{6\times n_k}, \quad k = a, b. \tag{6}$$

Operator $\tilde{\boldsymbol{r}}$ is the cross-product operator, i.e.,

$$\text{if} \quad \boldsymbol{r} = \begin{bmatrix} r_x \\ r_y \\ r_z \end{bmatrix}, \quad \text{then} \quad \tilde{\boldsymbol{r}} = \begin{bmatrix} 0 & -r_z & r_y \\ r_z & 0 & -r_x \\ -r_y & r_x & 0 \end{bmatrix}. \tag{7}$$

As is known to all, the whole on-orbit servicing task is composed of many stages, including far range rendezvous, close range rendezvous (is usually divided into two sub-phases: closing and final approach), station keeping, target capturing and repairing, *et al.* The space manipulator is only used in the capturing and repairing stages. Through station keeping, the position and orientation of the base with respect to the target can attain a relative ideal state, then the control of the base is turned off and the capturing stage starts. Therefore, when deducing the kinematic equations of free-floating space robot, it is general to assume that the initial values for linear and angular momentums are zeros. Many scholars have followed this assumption.[16,17,20,21,23,24]

Since no external forces and torques act on the free-floating system, the linear momentum and angular momentum are conserved. With the assumption that their initial values are zeros, the following equations are obtained:

$$\boldsymbol{P} = \sum_{i=0}^{n_a+n_b} m_i \dot{\boldsymbol{r}}_i = m_0 \boldsymbol{v}_0 + \sum_{i=1}^{n_a} m_i^a \dot{\boldsymbol{r}}_i^a + \sum_{i=1}^{n_b} m_i^b \dot{\boldsymbol{r}}_i^b = 0, \tag{8}$$

$$\boldsymbol{L} = \sum_{i=0}^{n_a+n_b} \left(\boldsymbol{I}_i \boldsymbol{\omega}_i + \dot{\boldsymbol{r}}_i \times m_i \dot{\boldsymbol{r}}_i\right) = 0, \tag{9}$$

where $\boldsymbol{P}$, $\boldsymbol{L}$ are, respectively, the linear and angular momentum of the system with respect to the inertial frame. Let $\boldsymbol{L}_0$ be the angular momentum of the system with respect to the mass center of the base, then the following relationship exists:

$$\boldsymbol{L} = \boldsymbol{L}_0 + \boldsymbol{r}_0 \times \boldsymbol{P}. \tag{10}$$

According to Eqs. (8) and (9),

$$\boldsymbol{L}_0 = 0. \tag{11}$$

Rearranging Eqs. (8) and (11) with $\boldsymbol{v}_0$, $\boldsymbol{\omega}_0$, and $\dot{\boldsymbol{\Theta}}$, we can get the following equation:

$$\begin{bmatrix} \boldsymbol{P} \\ \boldsymbol{L}_0 \end{bmatrix} = \begin{pmatrix} M\boldsymbol{E} & M\tilde{\boldsymbol{r}}_{0g}^T \\ M\tilde{\boldsymbol{r}}_{0g} & \boldsymbol{H}_w \end{pmatrix} \begin{bmatrix} \boldsymbol{v}_0 \\ \boldsymbol{\omega}_0 \end{bmatrix} + \begin{bmatrix} \boldsymbol{J}_{Tw}^a \\ \boldsymbol{H}_{w\phi}^a \end{bmatrix} \dot{\boldsymbol{\Theta}}^a + \begin{bmatrix} \boldsymbol{J}_{Tw}^b \\ \boldsymbol{H}_{w\phi}^b \end{bmatrix} \dot{\boldsymbol{\Theta}}^b = 0. \tag{12}$$

It can be described as

$$\boldsymbol{H}_b \dot{\boldsymbol{x}}_b + \boldsymbol{H}_{bm}^a \dot{\boldsymbol{\Theta}}^a + \boldsymbol{H}_{bm}^b \dot{\boldsymbol{\Theta}}^b = 0. \tag{13}$$

The matrixes $\boldsymbol{H}_b$ and $\boldsymbol{H}_{bm}$ are the inertia matrixes of the base and coupling inertia matrix, respectively. These are

https://doi.org/10.1017/S0263574711001007 Published online by Cambridge University Press

defined as follows:

$$\boldsymbol{H}_b = \begin{pmatrix} M\boldsymbol{E}_3 & M\tilde{\boldsymbol{r}}_{0g}^T \\ M\tilde{\boldsymbol{r}}_{0g} & \boldsymbol{H}_w \end{pmatrix} \in \boldsymbol{R}^{6x6}, \tag{14}$$

$$\boldsymbol{H}_{bm}^k = \begin{bmatrix} \boldsymbol{J}_{Tw}^k \\ \boldsymbol{H}_{w\phi}^k \end{bmatrix} \in \boldsymbol{R}^{6\times n_k}, \quad k = a, b, \tag{15}$$

$$\boldsymbol{H}_w = \sum_{i=1}^{n_a} \left(\boldsymbol{I}_i^a + m_i^a \left(\tilde{\boldsymbol{r}}_{0i}^a\right)^T \left(\tilde{\boldsymbol{r}}_{0i}^a\right)\right) + \sum_{i=1}^{n_b} \left(\boldsymbol{I}_i^b + m_i^b \left(\tilde{\boldsymbol{r}}_{0i}^b\right)^T \left(\tilde{\boldsymbol{r}}_{0i}^b\right)\right) + \boldsymbol{I}_0 \in \boldsymbol{R}^{3x3}, \tag{16}$$

$$\boldsymbol{H}_{w\phi}^k = \sum_{i=1}^{n_k} \left(\boldsymbol{I}_i^k \boldsymbol{J}_{Ri}^k + m_i^k \tilde{\boldsymbol{r}}_{0i}^k \boldsymbol{J}_{Ti}^k\right) \in \boldsymbol{R}^{3\times n_k}, \quad k = a, b, \tag{17}$$

$$\boldsymbol{J}_{Tw}^k = \sum_{i=1}^{n_k} \left(m_i^k \boldsymbol{J}_{Ti}^k\right) \in \boldsymbol{R}^{3\times n_k}, \quad k = a, b, \tag{18}$$

$$\boldsymbol{J}_{Ti}^k = \left[\boldsymbol{k}_1^k \times \left(\boldsymbol{r}_i^k - \boldsymbol{p}_1^k\right), \boldsymbol{k}_2^k \times \left(\boldsymbol{r}_i^k - \boldsymbol{p}_2^k\right), \ldots, \boldsymbol{k}_i^k \times \left(\boldsymbol{r}_i^k - \boldsymbol{p}_i^k\right), 0, \ldots, 0\right] \in \boldsymbol{R}^{3\times n_k}, \quad k = a, b, \tag{19}$$

$$\boldsymbol{J}_{Ri}^k = \left[\boldsymbol{k}_1^k, \boldsymbol{k}_2^k, \ldots, \boldsymbol{k}_i^k, 0, \ldots, 0\right] \in \boldsymbol{R}^{3\times n_k}, \quad k = a, b, \tag{20}$$

$$\boldsymbol{r}_{0g} = \boldsymbol{r}_g - \boldsymbol{r}_0, \tag{21}$$

$$\boldsymbol{r}_{0i}^k = \boldsymbol{r}_i^k - \boldsymbol{r}_0. \tag{22}$$

The linear velocity of the base can be solved by the first three rows of Eq. (12) (i.e., the linear momentum conservation equations):

$$\boldsymbol{v}_0 = -\tilde{\boldsymbol{r}}_{0g}^T \boldsymbol{\omega}_0 - \frac{\boldsymbol{J}_{Tw}^a \dot{\boldsymbol{\Theta}}^a + \boldsymbol{J}_{Tw}^b \dot{\boldsymbol{\Theta}}^b}{M} = \tilde{\boldsymbol{r}}_{0g}\boldsymbol{\omega}_0 - \frac{\boldsymbol{J}_{Tw}^a \dot{\boldsymbol{\Theta}}^a + \boldsymbol{J}_{Tw}^b \dot{\boldsymbol{\Theta}}^b}{M}. \tag{23}$$

Substituting Eq. (23) to the last three rows of Eq. (12), the following results are given:

$$\left(M\tilde{\boldsymbol{r}}_{0g}\tilde{\boldsymbol{r}}_{0g} + \boldsymbol{H}_w\right)\boldsymbol{\omega}_0 + \left(\boldsymbol{H}_{w\phi}^a - \tilde{\boldsymbol{r}}_{0g}\boldsymbol{J}_{Tw}^a\right)\dot{\boldsymbol{\Theta}}^a + \left(\boldsymbol{H}_{w\phi}^b - \tilde{\boldsymbol{r}}_{0g}\boldsymbol{J}_{Tw}^b\right)\dot{\boldsymbol{\Theta}}^b = 0. \tag{24}$$

Equation (24), i.e., the angular momentum conservation equation, can be written as

$$\boldsymbol{H}_s\boldsymbol{\omega}_0 + \boldsymbol{H}_\Theta^a\dot{\boldsymbol{\Theta}}^a + \boldsymbol{H}_\Theta^b\dot{\boldsymbol{\Theta}}^b = 0, \tag{25}$$

where

$$\boldsymbol{H}_s = \left(M\tilde{\boldsymbol{r}}_{0g}\tilde{\boldsymbol{r}}_{0g} + \boldsymbol{H}_w\right) \in \boldsymbol{R}^{3\times 3}, \tag{26}$$

$$\boldsymbol{H}_\Theta^k = \left(\boldsymbol{H}_{w\phi}^k - \tilde{\boldsymbol{r}}_{0g}\boldsymbol{J}_{Tw}^k\right) \in \boldsymbol{R}^{3\times n_k}, \quad k = a, b, \tag{27}$$

The matrix $\boldsymbol{H}_s$ is proved non-singular, so

$$\boldsymbol{v}_0 = -\left(\tilde{\boldsymbol{r}}_{0g}\boldsymbol{H}_s^{-1}\boldsymbol{H}_\Theta^a + \frac{\boldsymbol{J}_{Tw}^a}{M}\right)\dot{\boldsymbol{\Theta}}^a - \left(\tilde{\boldsymbol{r}}_{0g}\boldsymbol{H}_s^{-1}\boldsymbol{H}_\Theta^b + \frac{\boldsymbol{J}_{Tw}^b}{M}\right)\dot{\boldsymbol{\Theta}}^b, \tag{28}$$

$$\boldsymbol{\omega}_0 = -\boldsymbol{H}_s^{-1}\left(\boldsymbol{H}_\Theta^a\dot{\boldsymbol{\Theta}}^a + \boldsymbol{H}_\Theta^b\dot{\boldsymbol{\Theta}}^b\right). \tag{29}$$

The above two equations are combined as

$$\begin{bmatrix} \boldsymbol{v}_0 \\ \boldsymbol{\omega}_0 \end{bmatrix} = \boldsymbol{J}_{bm}^a\dot{\boldsymbol{\Theta}}^a + \boldsymbol{J}_{bm}^b\dot{\boldsymbol{\Theta}}^b = \begin{bmatrix} \boldsymbol{J}_{bm}^a & \boldsymbol{J}_{bm}^b \end{bmatrix}\begin{bmatrix} \dot{\boldsymbol{\Theta}}^a \\ \dot{\boldsymbol{\Theta}}^b \end{bmatrix} = \boldsymbol{J}_{bm}\begin{bmatrix} \dot{\boldsymbol{\Theta}}^a \\ \dot{\boldsymbol{\Theta}}^b \end{bmatrix}, \tag{30}$$

where

$$\boldsymbol{J}_{bm}^k = \begin{bmatrix} -\tilde{\boldsymbol{r}}_{0g}\boldsymbol{H}_s^{-1}\boldsymbol{H}_\Theta^k - \dfrac{\boldsymbol{J}_{Tw}^k}{M} \\ -\boldsymbol{H}_s^{-1}\boldsymbol{H}_\Theta^k \end{bmatrix}, \quad k = a, b, \tag{31}$$

$$\boldsymbol{J}_{bm} = \begin{bmatrix} \boldsymbol{J}_{bm}^a & \boldsymbol{J}_{bm}^b \end{bmatrix}. \tag{32}$$

Matrix $\boldsymbol{J}_{bm}^k(k = a, b)$ is the Jacobian matrix, mapping joint rates to the velocities (linear velocity and angular velocity) of the base. Substituting Eq. (30) to Eq. (4), the kinematic equations are given as

$$\begin{cases} \dot{\boldsymbol{x}}_e^a = \boldsymbol{J}_b^a\boldsymbol{J}_{bm}\begin{bmatrix} \dot{\boldsymbol{\Theta}}^a \\ \dot{\boldsymbol{\Theta}}^b \end{bmatrix} + \boldsymbol{J}_m^a\dot{\boldsymbol{\Theta}}^a \\ \dot{\boldsymbol{x}}_e^b = \boldsymbol{J}_b^b\boldsymbol{J}_{bm}\begin{bmatrix} \dot{\boldsymbol{\Theta}}^a \\ \dot{\boldsymbol{\Theta}}^b \end{bmatrix} + \boldsymbol{J}_m^b\dot{\boldsymbol{\Theta}}^b \end{cases}. \tag{33}$$

Equation (33) can be combined in the following form:

$$\begin{bmatrix} \dot{\boldsymbol{x}}_e^a \\ \dot{\boldsymbol{x}}_e^b \end{bmatrix} = \left(\begin{bmatrix} \boldsymbol{J}_b^a \\ \boldsymbol{J}_b^b \end{bmatrix}\boldsymbol{J}_{bm} + \begin{bmatrix} \boldsymbol{J}_m^a & \boldsymbol{O} \\ \boldsymbol{O} & \boldsymbol{J}_m^b \end{bmatrix}\right)\begin{bmatrix} \dot{\boldsymbol{\Theta}}^a \\ \dot{\boldsymbol{\Theta}}^b \end{bmatrix} = \boldsymbol{J}_g(\boldsymbol{\Psi}_b, \boldsymbol{\Theta}^a, \boldsymbol{\Theta}^b)\begin{bmatrix} \dot{\boldsymbol{\Theta}}^a \\ \dot{\boldsymbol{\Theta}}^b \end{bmatrix}, \tag{34}$$

where $\boldsymbol{J}_g \in \boldsymbol{R}^{12\times(n_a+n_b)}$ is the GJM of the dual-arm space robotic system.[17,25] It is the function of the spacecraft attitude, joint angles, and mass properties of each arm. When $n_a = n_b = 6$, $\boldsymbol{J}_g$ is a 12×12 square matrix. If $\boldsymbol{J}_g$ is non-singular, then the joint trajectories of the dual arm can be determined according to Eq. (34).

3. The Coordinated Motion Planning Methods

3.1. Dual-arm capturing when the base is free-floating

Generally, when the velocities of the end-effectors are given, the desired joint rates of the two arms can be solved according

https://doi.org/10.1017/S0263574711001007 Published online by Cambridge University Press

Table I. Numerical complexity in deriving the generalized vs. conventional Jacobians ($6 \times n$).

	Generalized Jacobian matrix	Conventional Jacobian matrix
Division	3 (3*)	0 (0*)
Multiplication	$13.5n^2 + 155.5n + 44$ (1463*)	$30n - 11$ (169*)
Addition & subtraction	$6n^2 + 141n + 17$ (1079*)	$18n - 20$ (88*)

*In case $n = 6$.

to Eq. (34),[17,18] i.e.,

$$\begin{bmatrix} \dot{\boldsymbol{\Theta}}_d^a \\ \dot{\boldsymbol{\Theta}}_d^b \end{bmatrix} = \boldsymbol{J}_g^{-1}(\boldsymbol{\Psi}_b, \boldsymbol{\Theta}^a, \boldsymbol{\Theta}^b) \begin{bmatrix} \dot{\boldsymbol{x}}_{ed}^a \\ \dot{\boldsymbol{x}}_{ed}^b \end{bmatrix}, \tag{35}$$

where $\dot{\boldsymbol{x}}_{ed}^a$ and $\dot{\boldsymbol{x}}_{ed}^b$ are the desired end-effectors' velocities, and $\dot{\boldsymbol{\Theta}}_d^a$ and $\dot{\boldsymbol{\Theta}}_d^b$ are the desired joint rates to realize the end-effectors' motion (i.e, $\dot{\boldsymbol{x}}_{ed}^a$ and $\dot{\boldsymbol{x}}_{ed}^b$) of arm-a and arm-b. The current states, i.e., $\boldsymbol{\Psi}_b$, $\boldsymbol{\Theta}^a$, and $\boldsymbol{\Theta}^b$, can be measured by corresponding sensors. However, there are $n_a + n_b$ (in this paper, $n_a = n_b = 6$) variables to be determined. The computation load is very large. In 1989, Masutani *et al.*[26,27] analyzed the computation load of GJM and compared it with that of a traditional Jacobian matrix based on same dimension. The important results are given as follows.

From then on "the computational cost for GJM is much more than that of the conventional Jacobians" became a consensus. In our paper, since the relative pose of the target, the attitude angles, rates of the base, the joint angles, and rates of the arms can be measured, we can use the approximate Jacobians, that is, the conventional Jacobians, which need only kinematic parameters and less computational cost. The proposed motion planning method belongs to that of resolved motion ration control (RMRC). In addition, the main computation load is the calculation of the Jacobian matrix and its inverse. Therefore, the comparison given in Table I can illustrate the computation effectiveness.

Moreover, the GJM $\boldsymbol{J}_g$ is a 12×12 square matrix and its singularities are much more complexly handled than those of a single-arm space robotic system. Since $\boldsymbol{J}_g$ is not only the function of the kinematic parameters but also the function of the mass properties (mass, inertia tensor, and mass center position of each body), the singularities are dynamic singularities,[19] which are dependent on the paths in Cartesian space. The characteristics complicate the Cartesian path planning of space robot. Therefore, we will partition the solution problem of Eq. (35) into two sub-problems with lower DOFs to simplify the singularity handling and reduce the computation load.

3.1.1. Simplification of kinematic equations. As pointed out above, the linear and angular momentums of free-floating system are conserved. By eliminating the holonomic constraints of linear momentum conservation, the total system is formulated as a nonholonomic system of $n_a + n_b + 3$ variables, including three dependent variables.[23]

Firstly, there exists the following relationship:

$$m_0 \boldsymbol{r}_0 + \sum_{i=1}^{n_a} m_i^a \boldsymbol{r}_i^a + \sum_{i=1}^{n_b} m_i^b \boldsymbol{r}_i^b = M \boldsymbol{r}_g, \tag{36}$$

where the system CM ($\boldsymbol{r}_g$) is fixed in inertia space. From Fig. 1, the CM of each link is

$$\boldsymbol{r}_i^k = \boldsymbol{r}_0 + \boldsymbol{b}_0^k + \sum_{j=1}^{i-1} \left(\boldsymbol{a}_j^k + \boldsymbol{b}_j^k \right) + \boldsymbol{a}_i^k. \tag{37}$$

In Eq. (37), $k = a, b;\ i = 1, 2, \ldots, n_k$. According to Eqs. (36) and (37), the base CM is determined by

$$\begin{aligned} \boldsymbol{r}_0 = \boldsymbol{r}_g &- \frac{\sum_{i=1}^{n_a} m_i^a \boldsymbol{b}_0^a}{M} - \frac{\sum_{i=1}^{n_b} m_i^b \boldsymbol{b}_0^b}{M} \\ &- \frac{\sum_{i=1}^{n_a} m_i^a \left(\sum_{j=1}^{i-1} \left(\boldsymbol{a}_j^a + \boldsymbol{b}_j^a \right) + \boldsymbol{a}_i^a \right)}{M} \\ &- \frac{\sum_{i=1}^{n_b} m_i^b \left(\sum_{j=1}^{i-1} \left(\boldsymbol{a}_j^b + \boldsymbol{b}_j^b \right) + \boldsymbol{a}_i^b \right)}{M}. \end{aligned} \tag{38}$$

Substituting Eq. (38) to Eq. (1), the position of the end-effector of arm-a is

$$\begin{aligned} \boldsymbol{p}_e^a &= \boldsymbol{r}_0 + \boldsymbol{b}_0^a + \sum_{i=1}^{n_a} \left(\boldsymbol{a}_i^a + \boldsymbol{b}_i^a \right) \\ &= \boldsymbol{r}_g + \frac{m_0 + \sum_{i=1}^{n_b} m_i^b}{M} \boldsymbol{b}_0^a - \frac{\sum_{i=1}^{n_b} m_i^b}{M} \boldsymbol{b}_0^b \sum_{i=1}^{n_a} \\ &\times \left(\frac{\sum_{q=0}^{i-1} m_q^a + \sum_{j=1}^{n_b} m_j^b}{M} \boldsymbol{a}_i^a + \frac{\sum_{q=0}^{i} m_q^a + \sum_{j=1}^{n_b} m_j^b}{M} \boldsymbol{b}_i^a \right) \\ &- \sum_{i=1}^{n_b} \left(\frac{\sum_{i}^{n_b} m_i^b}{M} \boldsymbol{a}_i^b + \frac{\sum_{i+1}^{n_b} m_i^b}{M} \boldsymbol{b}_i^b \right) \\ &= \boldsymbol{r}_g + \hat{\boldsymbol{b}}_0^a + \sum_{i=1}^{n_a} \left(\hat{\boldsymbol{a}}_i^a + \hat{\boldsymbol{b}}_i^a \right) - \breve{b}_0^b - \sum_{i=1}^{n_a} \left(\breve{a}_i^b + \breve{b}_i^b \right). \end{aligned} \tag{39}$$

Similarly, the position vector of the end-effector is

$$\boldsymbol{p}_e^b = \boldsymbol{r}_g + \hat{\boldsymbol{b}}_0^b + \sum_{i=1}^{n_b} \left(\hat{\boldsymbol{a}}_i^b + \hat{\boldsymbol{b}}_i^b \right) - \breve{b}_0^a - \sum_{i=1}^{n_a} \left(\breve{a}_i^a + \breve{b}_i^a \right), \tag{40}$$

where

$$\begin{cases} \hat{\boldsymbol{a}}_i^a = \dfrac{\sum_{q=0}^{i-1} m_q^a + \sum_{j=1}^{n_b} m_j^b}{M} \boldsymbol{a}_i^a, & i = 1, \ldots, n_a \\ \hat{\boldsymbol{b}}_i^a = \dfrac{\sum_{q=0}^{i} m_q^a + \sum_{j=1}^{n_b} m_j^b}{M} \boldsymbol{b}_i^a, & i = 0, \ldots, n_a \end{cases}, \tag{41}$$

https://doi.org/10.1017/S0263574711001007 Published online by Cambridge University Press

$$\begin{cases} \hat{\boldsymbol{a}}_i^b = \frac{\sum_{q=0}^{i-1} m_q^b + \sum_{j=1}^{n_a} m_j^a}{M} \boldsymbol{a}_i^b, \quad i = 1, \ \ldots, \ n_b \\ \hat{\boldsymbol{b}}_i^b = \frac{\sum_{q=0}^{i} m_q^b + \sum_{j=1}^{n_a} m_j^a}{M} \boldsymbol{b}_i^b, \quad i = 0, \ \ldots, \ n_b \end{cases}, \tag{42}$$

$$\begin{cases} \breve{a}i^k = \frac{\sum_{i}^{n_k} m_i^k}{M} \boldsymbol{a}_i^k, \ i = 1, \ \ldots, \ n_k \\ \breve{b}_i^k = \frac{\sum_{i+1}^{n_k} m_i^k}{M} \boldsymbol{b}_i^k, \ i = 0, \ \ldots, \ n_k \end{cases}, \quad k = a, b. \tag{43}$$

Vectors $\hat{\boldsymbol{a}}_i^k$, $\breve{a}_i^k$ and $\hat{\boldsymbol{b}}_i^k$, $\breve{b}_i^k$ are aligned with $\boldsymbol{a}_i^k$ and $\boldsymbol{b}_i^k$ $(k = a, b)$ respectively, and their lengths are constantly proportional to those of the corresponding vectors. Therefore, $\hat{\boldsymbol{a}}_i^k, \breve{a}_i^k$ and $\hat{\boldsymbol{b}}_i^k, \breve{b}_i^k$ are called "virtual link vectors." Differentiating the two sides of Eq. (39),

$$\begin{aligned} \boldsymbol{v}_e^a = \boldsymbol{v}_g + \boldsymbol{\omega}_0 \times \left(\hat{\boldsymbol{b}}_0^a - \tilde{\boldsymbol{b}}_0^b\right) + \sum_{i=1}^{n_a} \boldsymbol{\omega}_i^a \times \left(\hat{\boldsymbol{a}}_i^a + \hat{\boldsymbol{b}}_i^a\right) \\ - \sum_{i=1}^{n_b} \boldsymbol{\omega}_i^b \times \left(\breve{a}_i^b + \breve{b}_i^b\right), \end{aligned} \tag{44}$$

where $\boldsymbol{\omega}_i^k$ is the angular velocity of the ith body of arm-k $(k = a, b)$, which is calculated by

$$\boldsymbol{\omega}_i^k = \boldsymbol{\omega}_0 + \sum_{j=1}^{i} \boldsymbol{k}_j^k \dot{\theta}_j^k, \quad k = a, b. \tag{45}$$

Since there are no external forces on the system, with the assumption that the initial linear momentum is zero, the CM of the system keeps stationary, i.e., $\boldsymbol{v}_g = 0$. Hence, Eq. (44) can be simplified as

$$\begin{aligned} \boldsymbol{v}_e^a = -\left(\tilde{\hat{\boldsymbol{p}}}_{ge}^a - \tilde{\breve{p}}_{ge}^b\right)\boldsymbol{\omega}_0 + \sum_{i=1}^{n_a} \left[\boldsymbol{k}_i^a \times \left(\boldsymbol{p}_e^a - \hat{\boldsymbol{p}}_i^a\right)\right]\dot{\theta}_i^a \\ - \sum_{i=1}^{n_b} \left[\boldsymbol{k}_i^b \times \left(\boldsymbol{p}_e^b - \breve{p}_i^b\right)\right]\dot{\theta}_i^b. \end{aligned} \tag{46}$$

In Eq. (46)

$$\hat{\boldsymbol{p}}_{ge}^a = \hat{\boldsymbol{b}}_0^a + \sum_{i=1}^{n_a} \boldsymbol{A}_i^a \left({}^i\hat{\boldsymbol{a}}_i^a + {}^i\hat{\boldsymbol{b}}_i^a\right), \tag{47}$$

$$\breve{p}_{ge}^b = \breve{b}_0^b + \sum_{i=1}^{n_b} \boldsymbol{A}_i^b \left({}^i\breve{a}_i^b + {}^i\breve{b}_i^b\right), \tag{48}$$

$$\hat{\boldsymbol{p}}_i^a = \begin{cases} \boldsymbol{r}_g + \hat{\boldsymbol{b}}_0^a - \breve{b}_0^b - \sum_{i=1}^{n_a} \left(\breve{a}_i^b + \breve{b}_i^b\right), i = 1 \\ \boldsymbol{r}_g + \hat{\boldsymbol{b}}_0^a + \sum_{j=1}^{i-1} \left(\hat{\boldsymbol{a}}_j^a + \hat{\boldsymbol{b}}_j^a\right) - \breve{b}_0^b - \sum_{i=1}^{n_a} \left(\breve{a}_i^b + \breve{b}_i^b\right), \\ i > 1, \end{cases} \tag{49}$$

$$\breve{p}_i^b = \begin{cases} \boldsymbol{r}_g + \breve{b}_0^b - \breve{b}_0^a - \sum_{i=1}^{n_a} \left(\breve{a}_i^a + \breve{b}_i^a\right), i = 1 \\ \boldsymbol{r}_g + \breve{b}_0^b + \sum_{j=1}^{i-1} \left(\breve{a}_j^b + \breve{b}_j^b\right) - \breve{b}_0^a - \sum_{i=1}^{n_a} \left(\breve{a}_i^a + \breve{b}_i^a\right), \\ i > 1. \end{cases} \tag{50}$$

Then the differential kinematic equation of arm-a can be given by combining Eqs. (46) and (3):

$$\dot{\boldsymbol{x}}_e^a = \begin{bmatrix} \boldsymbol{v}_e^a \\ \boldsymbol{\omega}_e^a \end{bmatrix} = \hat{\boldsymbol{J}}_b^a \boldsymbol{\omega}_0 + \hat{\boldsymbol{J}}_m^a \dot{\boldsymbol{\Theta}}^a + \breve{J}_m^b \dot{\boldsymbol{\Theta}}^b \tag{51}$$

where

$$\hat{\boldsymbol{J}}_b^a = \begin{bmatrix} -\left(\tilde{\hat{\boldsymbol{p}}}_{ge}^a - \tilde{\breve{p}}_{ge}^b\right) \\ \boldsymbol{I}_3 \end{bmatrix} \in \boldsymbol{R}^{6\times 3}, \tag{52}$$

$$\hat{\boldsymbol{J}}_m^a = \begin{bmatrix} \boldsymbol{k}_1^a \times \left(\boldsymbol{p}_e^a - \hat{\boldsymbol{p}}_1^a\right) & \ldots & \boldsymbol{k}_n^a \times \left(\boldsymbol{p}_e^a - \hat{\boldsymbol{p}}_n^a\right) \\ \boldsymbol{k}_1^a & \ldots & \boldsymbol{k}_n^a \end{bmatrix} \in \boldsymbol{R}^{6\times n}, \tag{53}$$

$$\breve{J}_m^b = -\begin{bmatrix} \boldsymbol{k}_1^b \times \left(\boldsymbol{p}_e^b - \breve{p}_1^b\right) & \ldots & \boldsymbol{k}_n^b \times \left(\boldsymbol{p}_e^b - \breve{p}_n^b\right) \\ \boldsymbol{k}_1^b & \ldots & \boldsymbol{k}_n^b \end{bmatrix} \in \boldsymbol{R}^{6\times n}. \tag{54}$$

Similarly, the differential kinematic equation of arm-b can be described in the following form:

$$\dot{\boldsymbol{x}}_e^b = \begin{bmatrix} \boldsymbol{v}_e^b \\ \boldsymbol{\omega}_e^b \end{bmatrix} = \hat{\boldsymbol{J}}_b^b \boldsymbol{\omega}_0 + \breve{J}_m^a \dot{\boldsymbol{\Theta}}^a + \hat{\boldsymbol{J}}_m^b \dot{\boldsymbol{\Theta}}^b. \tag{55}$$

The corresponding vectors and matrixes are similar to those of arm-a. After the simplification of the motion equations, two important results are given, i.e., Eqs. (51) and (55), in which based on the law of the linear momentum conservation the linear velocity of the base's CM is eliminated.

3.1.2. The coordinated motion planning. (a) The main procedure: During the capturing, the hand-eye cameras supply the relative poses (position and attitude) of the target with respect to the end-effector on real-time. Based on the measured relative pose, the desired velocities (linear and angular velocities) of the two arms can be planned to capture the target in a coordinated behavior. Then the desired joint rates of arm-a and arm-b are generated according to the simplified differential kinematic equations, i.e., Eqs. (51) and (55).

The first case is that the base is free-floating, but its attitude angles and angular velocity are measured using some sensors – star sensors (or earth sensors) for attitude $\boldsymbol{\Psi}_b$ and gyroscope for angular velocity $\boldsymbol{\omega}_0$. They are generally mounted on a traditional satellite. Moreover, the two arms are equipped with potentiometers and encoders (each joint has a potentiometer and an encoder for backup and redundant purposes), which are used to measure the joint angles $(\boldsymbol{\Theta}^a, \ \boldsymbol{\Theta}^b)$ and rates $(\dot{\boldsymbol{\Theta}}^a, \ \dot{\boldsymbol{\Theta}}^b)$ (joint rates can be obtained by differentiating the joint angles).

The main steps of the planning method are as follows:

1. Set the stopping criteria, i.e., allowable range of the relative position and the orientation are $\varepsilon_p = 20$ mm and $\varepsilon_o = 2^\circ$, respectively, and the allowed maximal time is t_{max}.

https://doi.org/10.1017/S0263574711001007 Published online by Cambridge University Press

2. Measure the pose of the target relative to the end-effectors using the hand-eye cameras. The relative position and attitude are denoted by $\hat{\boldsymbol{r}}_{eh}^{k}$ and $\hat{\boldsymbol{\Psi}}_{eh}^{k}$ $(k = a, b)$.
3. Calculate the pose error (i.e., $\boldsymbol{e}_p^k$, $\boldsymbol{e}_o^k$) and judge whether the target lies within the capturing box (i.e., the grasp area, $\|\boldsymbol{e}_p^k\| \le \varepsilon_p$ and $\|\boldsymbol{e}_o^k\| \le \varepsilon_o$). If so, the manipulator closes its gripper and grasps the target; else, go to step 4.
4. Predict the target motion according to the measured values.
5. Read the current states (i.e., $\boldsymbol{\Psi}_b$, $\boldsymbol{\omega}_0$, $\boldsymbol{\Theta}^a$, $\dot{\boldsymbol{\Theta}}^a$, $\boldsymbol{\Theta}^b$, $\dot{\boldsymbol{\Theta}}^b$) of the space robotic system from the corresponding sensors.
6. Plan the end-effector velocities, which drive the end-effector to track and approach the target along the closest path (i.e., straight lines) using the measured and estimated results.
7. The singularity-avoiding algorithm is called to determine the desired joint angles and rates, i.e., $\boldsymbol{\Theta}_d^k$, $\dot{\boldsymbol{\Theta}}_d^k$.
8. The joint controllers generate driving torques of the joints to follow $\boldsymbol{\Theta}_d^k$ and $\dot{\boldsymbol{\Theta}}_d^k$.
9. $t = t + \Delta t$. If $t < t_{max}$, go to step 2; else, the algorithm stops, meaning that the space robot cannot capture the target in the prescribed time.

(b) The planning of the end-effector velocities: It is assumed that the measured results of the cameras are

$$\boldsymbol{r}_{eh}^{k} = [X,\ Y,\ Z]^T, \quad \boldsymbol{\Psi}_{eh}^{k} = [\alpha,\ \beta,\ \gamma]^T, \tag{56}$$

where $\boldsymbol{r}_{eh}^{k}$ and $\boldsymbol{\Psi}_{eh}^{k}$ are, respectively, the relative position and attitude supplied by camera-k, mounted on the end-effector of arm-k $(k = a, b)$.

The desired end-effector velocities are planned as follows:

$$\dot{\boldsymbol{x}}_{ed}^{k} = \begin{bmatrix} \boldsymbol{v}_{ed}^{k} \\ \boldsymbol{\omega}_{ed}^{k} \end{bmatrix} = \boldsymbol{K}^k \begin{bmatrix} \boldsymbol{r}_{eh}^{k} \\ \Delta \boldsymbol{O}^k \end{bmatrix} + \begin{bmatrix} \boldsymbol{v}_{h}^{k} \\ \boldsymbol{\omega}_{h}^{k} \end{bmatrix}, \tag{57}$$

where $\boldsymbol{v}_h^k$ and $\boldsymbol{\omega}_h^k$ are the estimated linear and angular velocities of the target, $\boldsymbol{K}^k$ is a matrix formed of the proportional coefficients used to limit the motion of the end-effector (in the paper, the bounds of the linear and angular velocities are 30 mm/s and 5°/s, respectively), and $\boldsymbol{\Delta O}^k$ is the orientation error, which is defined as

$$\begin{aligned} \Delta \boldsymbol{O}^k &= \frac{1}{2}\left(\boldsymbol{n}_e^k \times \boldsymbol{n}_h^k + \boldsymbol{o}_e^k \times \boldsymbol{o}_h^k + \boldsymbol{a}_e^k \times \boldsymbol{a}_h^k\right) \\ &= \frac{1}{2}\begin{bmatrix} \boldsymbol{A}_{eh}^k(2,3) - \boldsymbol{A}_{eh}^k(3,2) \\ -\boldsymbol{A}_{eh}^k(1,3) + \boldsymbol{A}_{eh}^k(3,1) \\ \boldsymbol{A}_{eh}^k(1,2) - \boldsymbol{A}_{eh}^k(2,1) \end{bmatrix}, \end{aligned} \tag{58}$$

where $[\boldsymbol{n}_e^k, \boldsymbol{o}_e^k, \boldsymbol{a}_e^k]$ and $[\boldsymbol{n}_h^k, \boldsymbol{o}_h^k, \boldsymbol{a}_h^k]$ are the rotation matrixes of $\sum_{ek}$ and $\sum_{hk}$, respectively. In addition, $\boldsymbol{A}_{eh}^k$ is the relative attitude matrix calculated according to the attitude angle $\boldsymbol{\Psi}_{eh}^k$. The pose errors used to judge whether the target is within the capturing box are calculated by

$$e_p^k = \left\|\boldsymbol{r}_{eh}^k\right\|, \quad e_o^k = \left\|\Delta \boldsymbol{O}^k\right\|. \tag{59}$$

(c) A practical approach to solve inverse kinematic: Equations (51) and (55) can be written in another form, i.e.,

$$\hat{\boldsymbol{J}}_m^a \dot{\boldsymbol{\Theta}}^a = \dot{\boldsymbol{x}}_e^a - \hat{\boldsymbol{J}}_b^a \boldsymbol{\omega}_0 - \breve{J}_m^b \dot{\boldsymbol{\Theta}}^b, \tag{60}$$

$$\hat{\boldsymbol{J}}_m^b \dot{\boldsymbol{\Theta}}^b = \dot{\boldsymbol{x}}_e^b - \hat{\boldsymbol{J}}_b^b \boldsymbol{\omega}_0 - \breve{J}_m^a \dot{\boldsymbol{\Theta}}^a. \tag{61}$$

The "current states of the system" at time t, i.e., $\boldsymbol{\Psi}_b(t)$, $\boldsymbol{\omega}_0(t)$, $\boldsymbol{\Theta}^a(t)$, $\dot{\boldsymbol{\Theta}}^a(t)$, $\boldsymbol{\Theta}^b(t)$, $\dot{\boldsymbol{\Theta}}^b(t)$, can be supplied by the sensors. So "the desired states at next sample time," i.e., $\boldsymbol{\Theta}_d^a(t + \Delta t)$, $\boldsymbol{\Theta}_d^b(t + \Delta t)$ and $\boldsymbol{\Theta}_d^b(t + \Delta t)$, $\dot{\boldsymbol{\Theta}}_d^b(t + \Delta t)$, can be recursively planned according to the desired velocities of the end-effectors on real-time. Equation (60) is slightly modified in the following form (Eq. (61) will be handled in a similar way):

$$\hat{\boldsymbol{J}}_m^a \dot{\boldsymbol{\Theta}}_d^a(t + \Delta t) = \dot{\boldsymbol{x}}_{ed}^a(t + \Delta t) - \hat{\boldsymbol{J}}_b^a \boldsymbol{\omega}_0(t) - \breve{J}_m^b \dot{\boldsymbol{\Theta}}^b(t). \tag{62}$$

The vectors in Eq. (62), described in the inertial frame, are then transformed to the body-fixed frame of the base by multiplying matrix $\mathrm{diag}(\boldsymbol{A}_0^T,\ \boldsymbol{A}_0^T)$, i.e.,

$${}^0\hat{\boldsymbol{J}}_m^a \dot{\boldsymbol{\Theta}}_d^a(t + \Delta t) = {}^0\dot{\boldsymbol{x}}_{ed}^a(t + \Delta t) - {}^0\hat{\boldsymbol{J}}_b^a \boldsymbol{\omega}_0(t) - {}^0\breve{J}_m^b \dot{\boldsymbol{\Theta}}^b(t). \tag{63}$$

The right side of Eq. (63) is actually the end-effector velocity with relative to the base (expressed in the base frame) and denoted by

$${}^0\dot{\boldsymbol{y}}_{ed}^a(t + \Delta t) = {}^0\dot{\boldsymbol{x}}_{ed}^a(t + \Delta t) - {}^0\hat{\boldsymbol{J}}_b^a \boldsymbol{\omega}_0(t) - {}^0\breve{J}_m^b \dot{\boldsymbol{\Theta}}^b(t). \tag{64}$$

So, Eq. (63) can be written as

$${}^0\hat{\boldsymbol{J}}_m^a \dot{\boldsymbol{\Theta}}_d^a(t + \Delta t) = {}^0\dot{\boldsymbol{y}}_{ed}^a(t + \Delta t), \tag{65}$$

where ${}^0\dot{\boldsymbol{y}}_{ed}^a(t + \Delta t)$ is the desired velocity with respect to the base. From Eq. (53), ${}^0\hat{\boldsymbol{J}}_m^a$ is independent on dynamic parameters. Therefore, the singularities of ${}^0\hat{\boldsymbol{J}}_m^a$ are kinematic. Then the dynamic singularity-handling problem is transformed into real-time kinematic singularity avoiding problem. It should be pointed out that the dynamic singularity points in the task space and cannot be identified beforehand. However, when the angular velocity and attitude of the base are measured on real-time (at each sampling period), a simplified kinematic equation, i.e., Eq. (65), is derived. Equations (62)–(65) show that the desired inertial motion of the end-effector ($\dot{\boldsymbol{x}}_{ed}^a$) at time $t + \Delta t$ can be realized by the planned joint motion ($\dot{\boldsymbol{\Theta}}_d^a$) according to Eq. (65), using the states of the space robotic system at time t. It is undeniable that compared with the results given by the ideal relationship (i.e., Eq. (35)) there are certain errors, because the states at $t + \Delta t$ are little different from the states at t. However, if Δt is short enough, or the desired motion is slow, the errors will not be large and can be neglected. In addition, the actual relative pose between the end-effector and the target can be measured on real-time, which means that the errors will not cumulate.

To solve Eq. (65), there only exist kinematic singularities. In order to easily explain the singularity avoidance concept, a Puma-like robot (wrist-partitioned manipulator) is used as an

https://doi.org/10.1017/S0263574711001007 Published online by Cambridge University Press

example (although wrist-partitioned space manipulators are taken as the example, the approaches can be easily extended to other types of manipulators). According to the definitions of Jacobian matrixes, the following relationship exists:

$$\left({}^0\hat{\boldsymbol{J}}_m^a\right) = \begin{bmatrix} \boldsymbol{I} & -\left(\hat{L}_6^a + \hat{L}_7^a\right)\tilde{\boldsymbol{Z}}_6^a \\ \boldsymbol{O} & \boldsymbol{I} \end{bmatrix} \left({}^0\hat{\boldsymbol{J}}_W^a\right), \tag{66}$$

where $\hat{L}_6^a + \hat{L}_7^a$ is the length from the wrist center to the end-effector of the virtual manipulator. ${}^0\hat{\boldsymbol{J}}_W^a$ is the wrist-reference Jacobian matrix, establishing relationship between the joint rates and wrist velocities. It is of the following form:

$${}^0\hat{\boldsymbol{J}}_W^a = \begin{bmatrix} {}^0\hat{\boldsymbol{J}}_{11}^a & \boldsymbol{O}_{3\times 3} \\ {}^0\hat{\boldsymbol{J}}_{21}^a & {}^0\hat{\boldsymbol{J}}_{22}^a \end{bmatrix}. \tag{67}$$

Then the method "Singularity Separation Plus Damped Reciprocal" (SSPDR), proposed by the authors,[28] are used to handle the singularities.

The desired joint rates of arm-b are also determined using the similar method to solve the following equation:

$${}^0\hat{\boldsymbol{J}}_m^b \dot{\boldsymbol{\Theta}}_d^b(t+\Delta t) = {}^0\dot{\boldsymbol{y}}_{ed}^b(t+\Delta t), \tag{68}$$

where

$${}^0\dot{\boldsymbol{y}}_{ed}^b(t+\Delta t) = {}^0\dot{\boldsymbol{x}}_{ed}^b(t+\Delta t) - {}^0\hat{\boldsymbol{J}}_b^b\boldsymbol{\omega}_0(t) - {}^0\breve{J}_m^a\dot{\boldsymbol{\Theta}}^a(t). \tag{69}$$

3.2. The single-arm capturing while keeping the base's inertial pose

3.2.1. The existing problems of traditional methods. For some applications, the two arms can be used as the mission arm and the balance arm. The mission arm is used to accomplish desired mission and the balance arm is used to compensate the attitude of the base using the dynamics coupling characteristic. Furthermore, the balance arm can be designed to maintain the base approximately fixed in the inertial pose during the manipulation of the mission arm. Agrawal *et al*[21]. derived the necessary mathematical conditions and implemented some algorithms for motion planning in joint coordinates and Cartesian coordinates. But the singularities are important problems needed to be solved further.

The momentum conservation equations of the free-floating space robot are rewritten here to illuminate the concept, i.e.,

$$\boldsymbol{H}_b\dot{\boldsymbol{x}}_b + \boldsymbol{H}_{bm}^a\dot{\boldsymbol{\Theta}}^a + \boldsymbol{H}_{bm}^b\dot{\boldsymbol{\Theta}}^b = 0. \tag{70}$$

In order to keep the base fixed inertially, i.e., $\dot{\boldsymbol{x}}_b = 0$, the following condition must be satisfied:

$$\boldsymbol{H}_{bm}^a\dot{\boldsymbol{\Theta}}^a + \boldsymbol{H}_{bm}^b\dot{\boldsymbol{\Theta}}^b = 0. \tag{71}$$

If arm-a is used as the mission arm, $\dot{\boldsymbol{\Theta}}_d^a$ is planned according to the requirement of the mission. Then the joint rates of the balance arm are determined by

$$\dot{\boldsymbol{\Theta}}_d^b = -\left(\boldsymbol{H}_{bm}^b\right)^{-1}\boldsymbol{H}_{bm}^a\dot{\boldsymbol{\Theta}}_d^a. \tag{72}$$

Unfortunately, $\boldsymbol{H}_{bm}^b$ is a possible singularity for some cases. Agrawal *et al.*[21] used the algorithms based on position kinematics of the system coupled with the iterative procedure to satisfy the nonholonomic constraints and avoid singularities during motion. However, the scheme implemented for the planar dual-arm, free-floating system will be much more complex for higher DOF systems, such as the case studied in this paper. So we propose an approach with which the balance arm is mainly used to maintain the inertial position of the base's centroid, and the reaction wheels are used to absorb the resultant angular momentums generated by the two arms' motion. This method is detailed in the following parts. The linear momentum conservation equation (i.e., Eq. (8)) and the angular momentum conservation equation (i.e., Eq. (25)) are handled respectively. Equation (8) or its position form (Eq. (36)) is used to simplify the kinematic equations (Section 3.1.1) and plan the coordinated motion of the balance arm (Section 3.2.1). In addition, Eq. (25) is used to plan the desired angular speed of the reaction wheels to absorb the resultant angular momentums generated by the two arms' motion. This method is detailed in the following parts.

3.2.2. The trajectory planning of the mission arm and balance arm. Firstly, the motion of arm-a is autonomously planned to capture the target according to the measurements of the camera mounted on its end-effector. Since the base is inertially fixed, the linear and angular velocities are approximately zero, i.e.,

$$\boldsymbol{v}_0 \approx 0, \quad \boldsymbol{\omega}_0 \approx 0. \tag{73}$$

Submitting Eq. (73) to Eq. (4), the following equation can be used to determine the desired joint rates of arm-a:

$$\dot{\boldsymbol{x}}_{ed}^a = \boldsymbol{J}_m^a\dot{\boldsymbol{\Theta}}_d^a. \tag{74}$$

Equation (74) is same as the traditional kinematic equation of the base-fixed manipulator, and the SSPDR method is directly used to handle the singularity problems.

The linear momentum conservation equation is a holonomic constraint and can be written in the following position form:

$$m_0\boldsymbol{r}_0 + \sum_{i=1}^{n_a} m_i^a\boldsymbol{r}_i^a + \sum_{i=1}^{n_b} m_i^b\boldsymbol{r}_i^b = m_0\boldsymbol{r}_0 + M_a\boldsymbol{r}_{\sum}^a + M_b\boldsymbol{r}_{\sum}^b = 0, \tag{75}$$

where $M_a = \sum_{i=1}^{n_a} m_i^a$ and $M_b = \sum_{i=1}^{n_b} m_i^b$ are the total mass of arm-a and arm-b, respectively, and $\boldsymbol{r}_{\sum}^a$ and $\boldsymbol{r}_{\sum}^b$ are their equivalent centroids. Then the system is considered as three parts: the base, arm-a, and arm-b. If the total system, including the base and the two arms, are elaborately designed,

https://doi.org/10.1017/S0263574711001007 Published online by Cambridge University Press

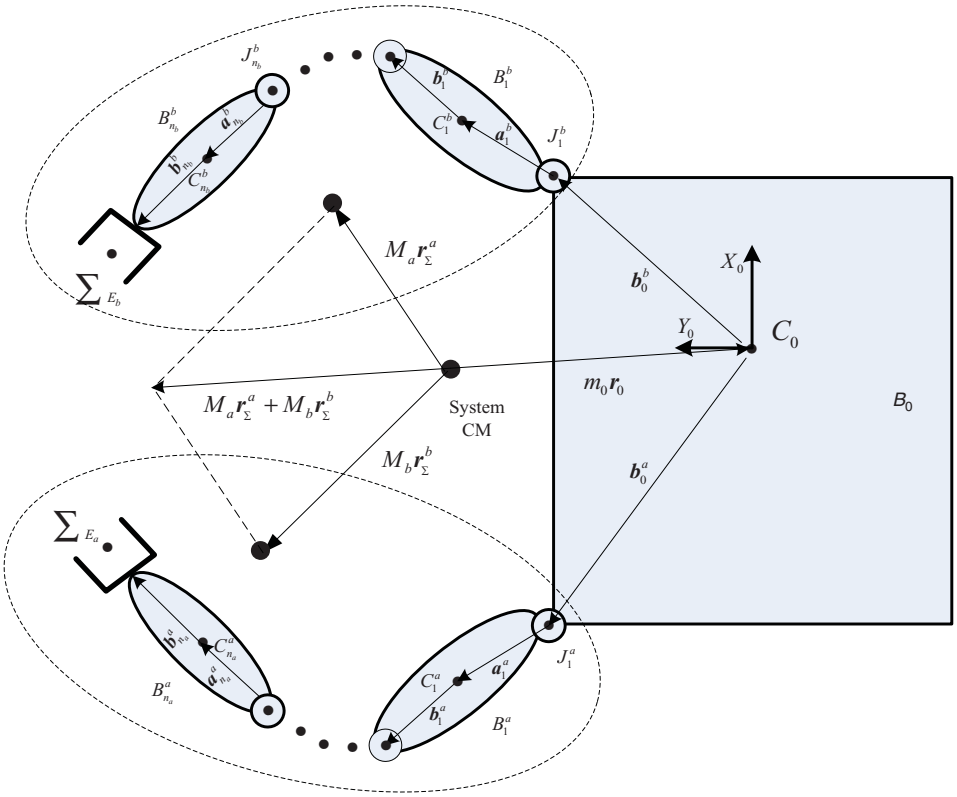

Fig. 2. (Colour online) The positional relationship of the centroid of the two arms and base.

it is possible to satisfy the following condition during motion:

$$M_a\boldsymbol{r}_\Sigma^a + M_b\boldsymbol{r}_\Sigma^b = 0. \tag{76}$$

Then the base's CM is fixed at $\boldsymbol{r}_0 = 0$, derived from Eq. (75). This concept is shown in Fig. 2.

Here we design two full identical arms and mounted centrosymmetrically with respect to the centroid of the base. When the joints of arm-b move with same trajectories as those of arm-a, i.e.,

$$\dot{\boldsymbol{\Theta}}_d^b = \dot{\boldsymbol{\Theta}}_d^a, \tag{77}$$

condition (76) is naturally satisfied, and $\boldsymbol{r}_0$ will be constant during the motion.

It should be pointed out that Eq. (77) is not directly deduced from Eq. (72). The precondition of utilizing Eq. (77) is that "the two arms are fully identical and mounted centrosymmetrically with respect to the centroid of the base." When this precondition is satisfied, $\dot{\boldsymbol{\Theta}}_d^b = \dot{\boldsymbol{\Theta}}_d^a$ will always make $M_a\boldsymbol{r}_\Sigma^a + M_b\boldsymbol{r}_\Sigma^b = \text{const}$. Correspondingly, r_0 will always remain constant (in fact, r_0 will have tiny variation for the reason that the joint control errors exist). By elaborately designing and arranging the two arms and the base, the second task in the paper can be easily completed.

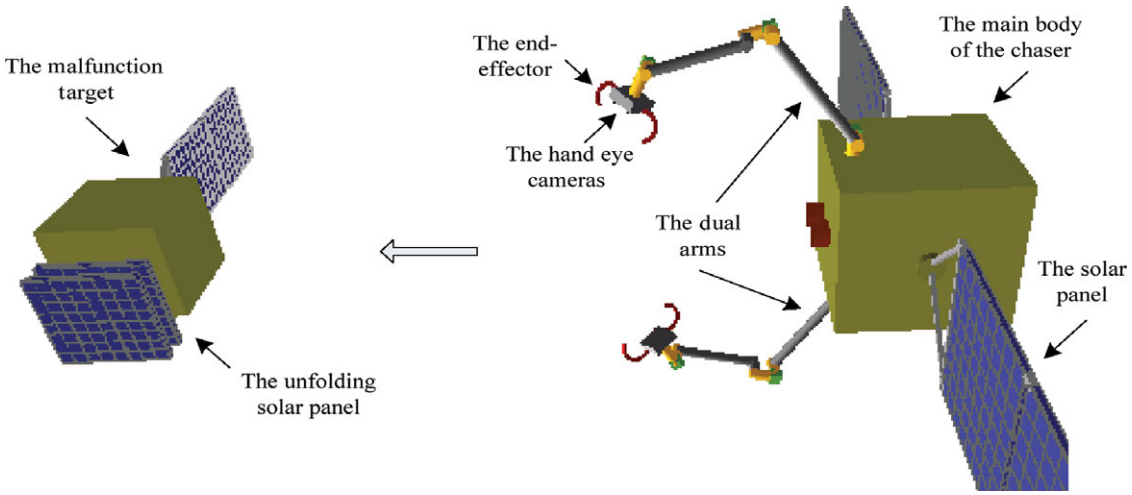

Fig. 3. (Colour online) The dual-arm space robotic system and the malfunctioned satellite.

https://doi.org/10.1017/S0263574711001007 Published online by Cambridge University Press

Table II. The mass properties of the space robotic system.

		B_0	B_1	B_2	B_3	B_4	B_5	B_6
Mass (kg)		1000	13	10	13	10	13	12
${}^i\boldsymbol{a}_i$/m		0.6	0	−0.493	0.026	0.391	−0.026	−0.189
		0	−0.012	0.145	−0.070	−0.144	0.070	0
		0	0.097	0	0	0	0	0.023
${}^i\boldsymbol{b}_i$/m		0.5	0	−0.357	0.032	0.573	−0.032	−0.099
		0	0.070	−0.145	0.012	0.086	−0.012	0
		0.712	0.026	0	0	0	0	−0.023
${}^i\boldsymbol{I}_i$ ($kg.m^2$)	I_{xx}	490	0.113	0.034	0.069	0.633	0.227	0.212
	I_{yy}	520	0.136	1.387	0.226	0.567	0.069	0.210
	I_{zz}	510	0.059	1.382	0.203	0.093	0.203	0.208
	I_{yx}	1.341	0	0	0	0	0	0
	I_{zx}	0.116	−0.008	0	−0.006	0	0	0
	I_{zy}	0.158	0	0	0	0.202	0.008	0

The condition "two arms are fully identical and mounted centrosymmetrically with respect to the centroid of the base" is only an example, which always satisfies Eq. (76) when using Eq. (77) to generate the motion of the counter arm. In fact, Eq. (76) can be written in the following form:

$$M_a \boldsymbol{r}^a_{\sum}(\boldsymbol{\Theta}_a) + M_b \boldsymbol{r}^b_{\sum}(\boldsymbol{\Theta}_b) = 0, \tag{78}$$

where $\boldsymbol{r}^a_{\sum}(\boldsymbol{\Theta}_a)$ and $\boldsymbol{r}^b_{\sum}(\boldsymbol{\Theta}_b)$ show that $\boldsymbol{r}^a_{\sum}$ and $\boldsymbol{r}^b_{\sum}$ are, respectively, the functions of $\boldsymbol{\Theta}_a$ and $\boldsymbol{\Theta}_b$. If the motion of arm-b is planned to satisfy the above equation, the position of the base satellite's centroid will be fixed in the inertial frame during the mission. Since Eq. (76) is independent on specific configuration, the proposed method can also be used for other cases except for the example "two arms are fully identical and mounted centrosymmetrically with respect to the centroid of the base." However, we can simplify the planning algorithm by elaborately designing the counter arm, as shown by the given example.

3.2.3. The motion planning of reaction wheels. Although a balance arm can be designed to keep the inertial position of the base's CM, the resultant angular momentum of arm-a and arm-b will be not zero. Therefore, in order to maintain the orientation of the base to be fixed inertially, the reaction wheels are used to compensate the resultant angular momentum. The angular momentum conservation Eq. (25) is then modified as ($\boldsymbol{\omega}_0 \approx \boldsymbol{O}$):

$$\boldsymbol{H}^a_{\Theta}\dot{\boldsymbol{\Theta}}^a_d + \boldsymbol{H}^b_{\Theta}\dot{\boldsymbol{\Theta}}^b_d + \boldsymbol{H}_w\boldsymbol{\Omega} = 0, \tag{79}$$

where $\boldsymbol{H}_w = \mathrm{diag}(I_{w_x},\ I_{w_y},\ I_{w_z})$ and $\boldsymbol{\Omega} = [\Omega_x,\ \Omega_y,\ \Omega_z]^T$ are, respectively, the inertial matrix and rotation speed vector composed of the corresponding component of the flywheels. Then the motion of the flywheels can be determined by

$$\boldsymbol{\Omega} = \boldsymbol{H}_w^{-1}\left(\boldsymbol{H}^a_{\Theta}\dot{\boldsymbol{\Theta}}^a_d + \boldsymbol{H}^b_{\Theta}\dot{\boldsymbol{\Theta}}^b_d\right). \tag{80}$$

If the reaction wheels are controlled to realize the motion given in Eq. (80), then the base will be stabilized at its initial orientation.

4. Simulation Study

4.1. The designed dual-arm space robot system

The target to be serviced is assumed to be a malfunctioned satellite, one of whose solar panels is unfolded. The designed space robotic system used for the on-orbit servicing mission is shown as Fig. 3. It is composed of a carrier spacecraft (called *space base* or *base*) and two 6DOFs PUMA-type manipulators (called *space manipulators*, which are denoted as arm-a and arm-b). The two arms are identical, that is to say, they have the same geometry and mass properties. However, they are mounted at different positions. Table II lists the dimensions and mass properties of the bodies (*Sat* and B_i stand for the satellite and the ith body, respectively).

The control system of the space manipulator is a typical distributed control system (DCS); its structure is shown in Fig. 4. It is composed of a coordinated planner, 12 joint controllers (JC; six for each arm), two hand-eye end-effector controllers (one for each arm), and two hand-eye camera processors (one for each arm). The coordinated planner receives instructions from the ground or other subsystems, such as GNC subsystem, data-handling subsystem, etc.; then it plans the trajectories of the manipulator joints. Limited by the computation abilities of the on-board processors, the communication frequency between subsystems through Controller Area Network (CAN) bus is about 4 Hz. On the other hand, the control cycle of the joint controller, whose control law is Proportional-Integral-Derivative (PID), is lower than 5 ms (control frequency is about 200 Hz). Each JC autonomously interposes more position nodes using a certain polynomial function. Here the 3rd spline function is used.

4.2. Simulation for dual-arm capturing when the base is free-floating

A typical on-orbit servicing mission is conducted in a series of operations: far-range rendezvous, close-range rendezvous (it is usually divided into two sub-phases: closing and final approach), station keeping, target capturing, and repairing. The space manipulator is only used in the capturing and repairing stages. Through station keeping, the position and orientation of the base with respect to target can attain a relative ideal state, then the control of the base is turned off

https://doi.org/10.1017/S0263574711001007 Published online by Cambridge University Press

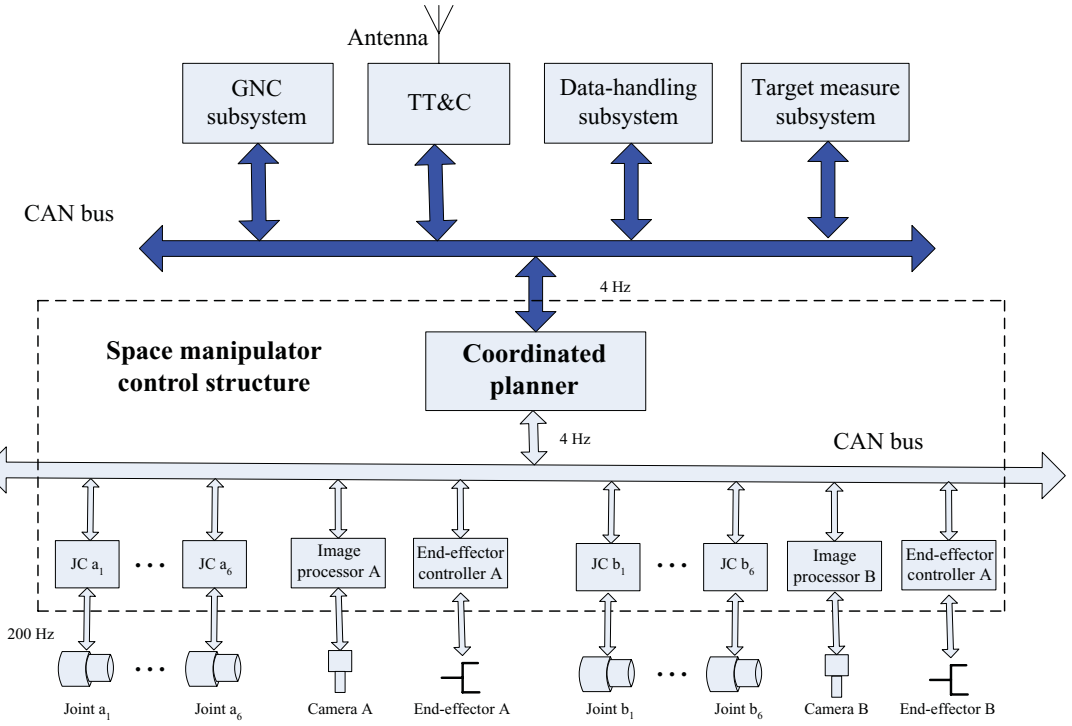

Fig. 4. (Colour online) The control structure of the space manipulator.

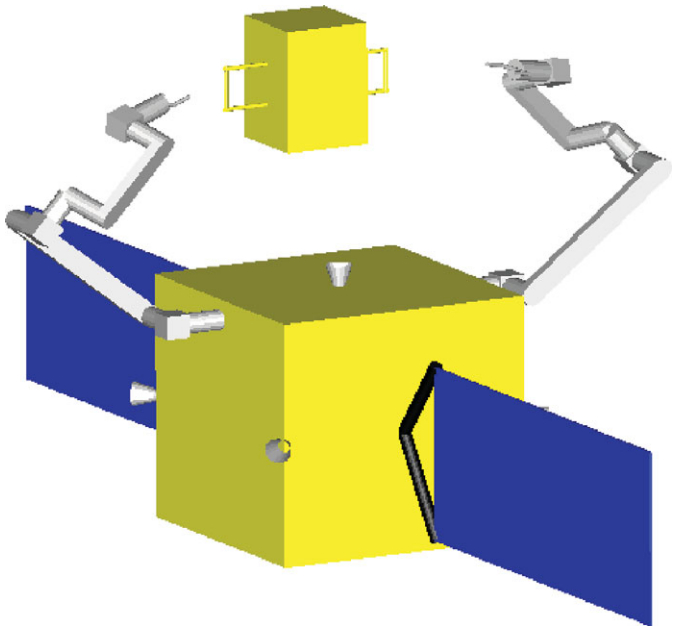

Fig. 5. (Colour online) The initial state when capturing the target.

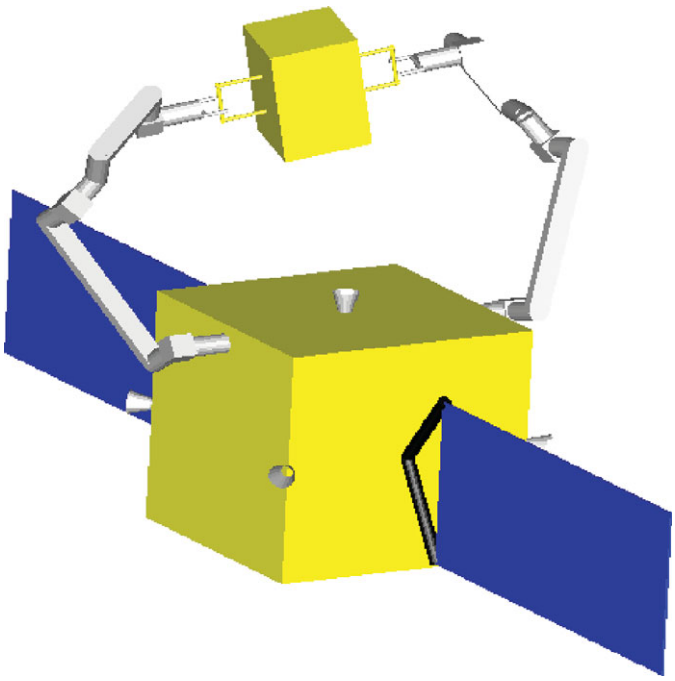

Fig. 6. (Colour online) The final state when capturing the target.

and the capturing stage starts. In this paper, we focus on the target capturing and assume that the station keeping stage is finished, which means that the relative linear and angular speeds of the target will not be very large.

According to the target capturing demonstrated on ETS-VII and Orbital Express, the space robot will move toward the approach corridor from a far range, where the arm is first commanded to the ready-capture configuration, which positioned the tip of the arm above a virtual capture-box attached to the arm base frame. The space robot has to position itself so that the target handle was in the capture-box, within specified relative rates, prior to initiation of visual servo. Once the space robot positioned itself so that the target is within the capture-box, the arms will have a clear view of the target with its hand-eye cameras. The arms' vision systems are then commanded to acquire the visual features on the target. Once the target feature is acquired, the space robot transitions to free-floating, and the arms are controlled in visual servo mode to capture the target. As for the selection of the ready-capture configuration, the main factors needing consideration include common

https://doi.org/10.1017/S0263574711001007 Published online by Cambridge University Press

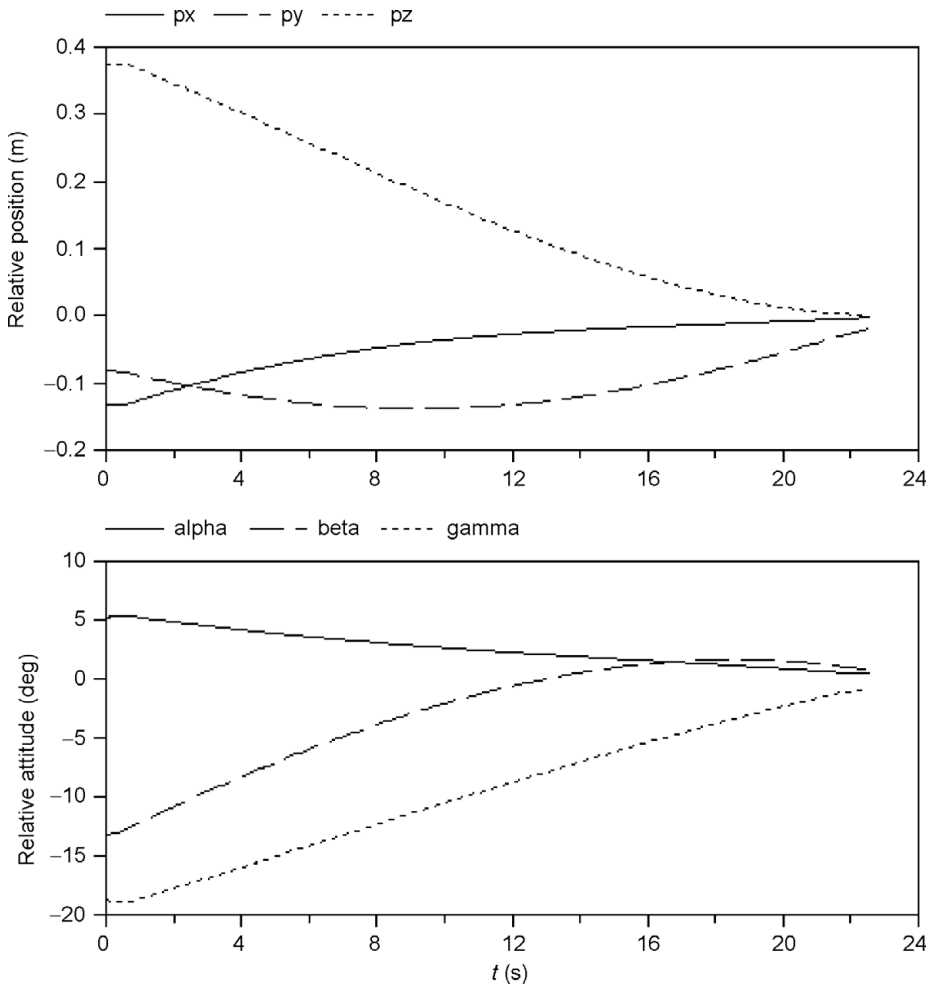

Fig. 7. The variation curves of the relative pose of arm-a.

capture-box range (it is determined by the geometry dimension and mounted pose) of the two arms, the station-keeping ability (relative pose and rate) of the space robot, and the measure range of the hand-eye cameras. For the space robot designed in Section 4.1, the ready-capture configurations of the two arms are as under:

$$\begin{aligned}&\boldsymbol{\Theta}_0^a = \boldsymbol{\Theta}_0^b \\ &= [0^\circ, \quad -130.00^\circ, \quad 88.75^\circ, \quad -30^\circ, \quad -218.76^\circ, \quad -25^\circ]^T.\end{aligned} \tag{81}$$

The initial attitude of the base is assumed as

$$\boldsymbol{\Psi}_{b0} = [0 \quad 0 \quad 0]^T. \tag{82}$$

The CM frame of the target, and the poses of the handles mounted on the target (with respect to $\sum_B$) are, respectively, as follows:

$$\begin{aligned}\boldsymbol{X}_t = [&2.1480\,\text{m}, \quad 0.30\,\text{m}, \quad 0.0\,\text{m}, \quad 0.00^\circ, \quad 0.00^\circ, \\ &0.00^\circ]^T,\end{aligned} \tag{83}$$

$$\begin{aligned}\boldsymbol{X}_{h0}^a = \big[&2.1480\,\text{m}, \quad 0.30\,\text{m}, \quad 0.4\,\text{m}, \quad 0.00^\circ, \quad 0.00^\circ, \\ &0.00^\circ]^T,\end{aligned} \tag{84}$$

$$\begin{aligned}\boldsymbol{X}_{h0}^b = \big[&2.1480\,\text{m}, \quad 0.30\,\text{m}, \quad -0.4\,\text{m}, \quad 0.00^\circ, \quad 0.00^\circ, \\ &0.00^\circ]^T.\end{aligned} \tag{85}$$

As discussed above, the target capturing stage will not start until the station keeping condition is satisfied. That is to say, the maximum relative linear and angular velocities between the tip of the arm and the grapple fixture on the target prior to the initiation of arm motion for free-flyer capture are controlled within specified limits. When these conditions are satisfied, the visual feature and grapple fixture on the target are within the field of view of the cameras mounted on the arm end-effector. According to the experiences of the Orbital Express[29–31] and ETS-VII, the target CM is assumed to move with constant velocities (moderate velocities):

$$\begin{aligned}\boldsymbol{v}_t &= [5\,\text{mm/s}, \ 5\,\text{mm/s}, \ -5\,\text{mm/s}]^T, \\ \boldsymbol{\omega}_t &= [-0.5^\circ/\text{s}, \ -0.5^\circ/\text{s}, \ -0.5^\circ/\text{s}]^T.\end{aligned} \tag{86}$$

The plus or minus sign is set according to worse case for the target capturing, i.e., the target moves apart from the base.

The initial state determined by Eqs. (81)–(85) is three-dimensional as displayed in Fig. 5. The coordinated motion approaches proposed in Section 3 are used to plan the trajectories of the two arms. The velocities of the end-effector

https://doi.org/10.1017/S0263574711001007 Published online by Cambridge University Press

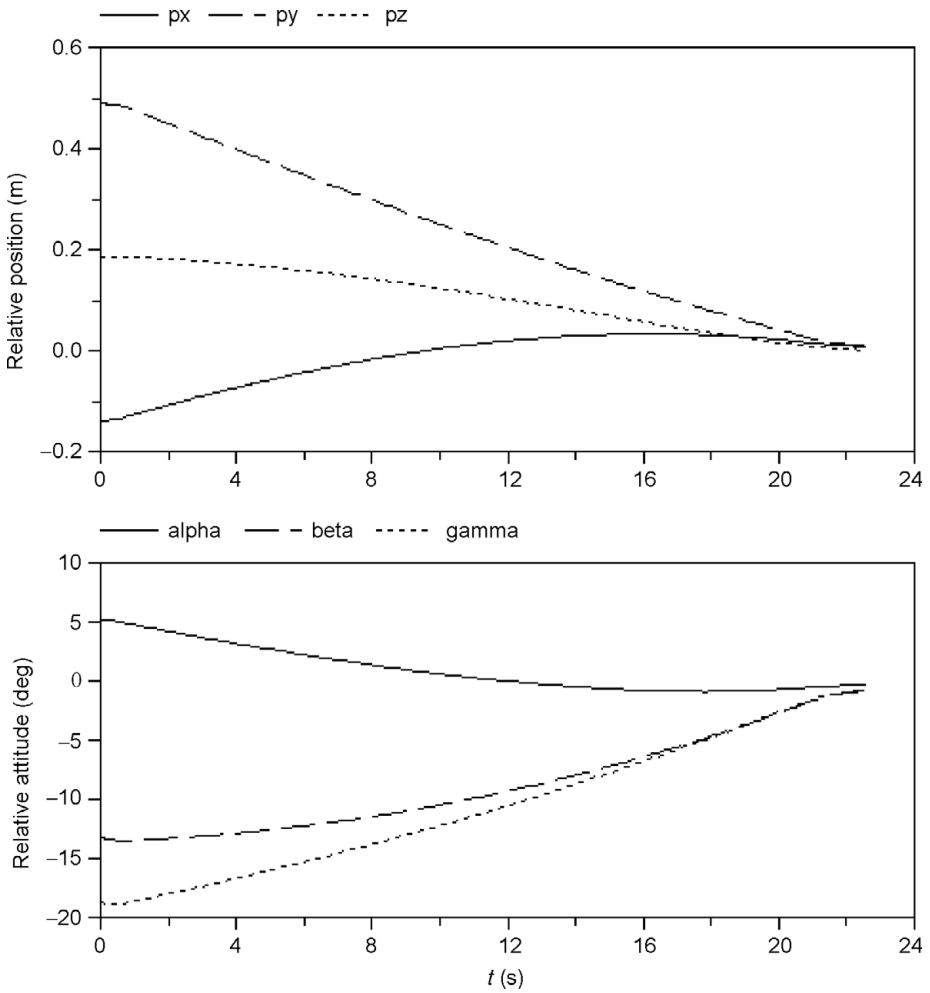

Fig. 8. The variation curves of the relative pose of arm-b.

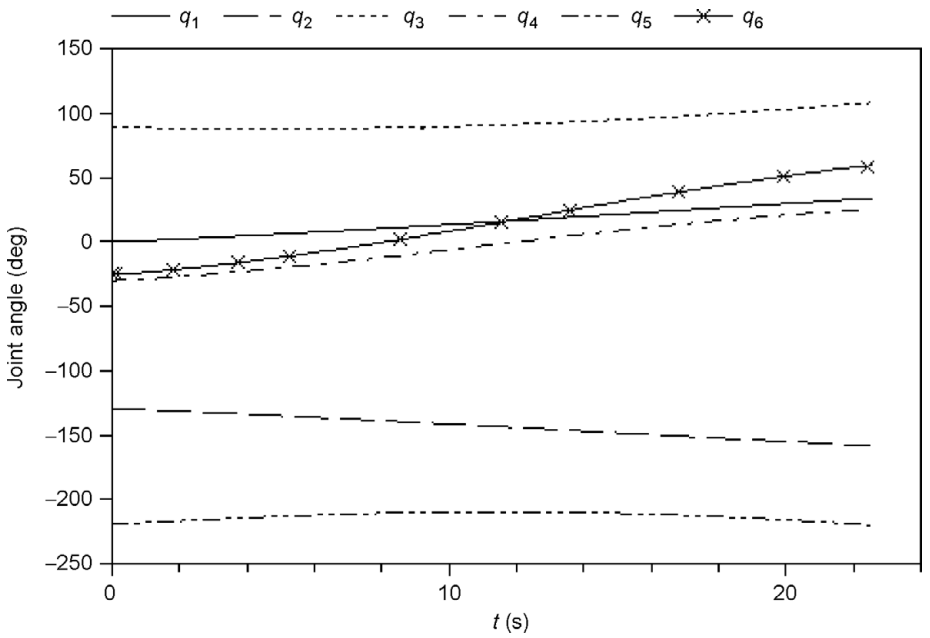

Fig. 9. The joint trajectories of arm-a.

https://doi.org/10.1017/S0263574711001007 Published online by Cambridge University Press

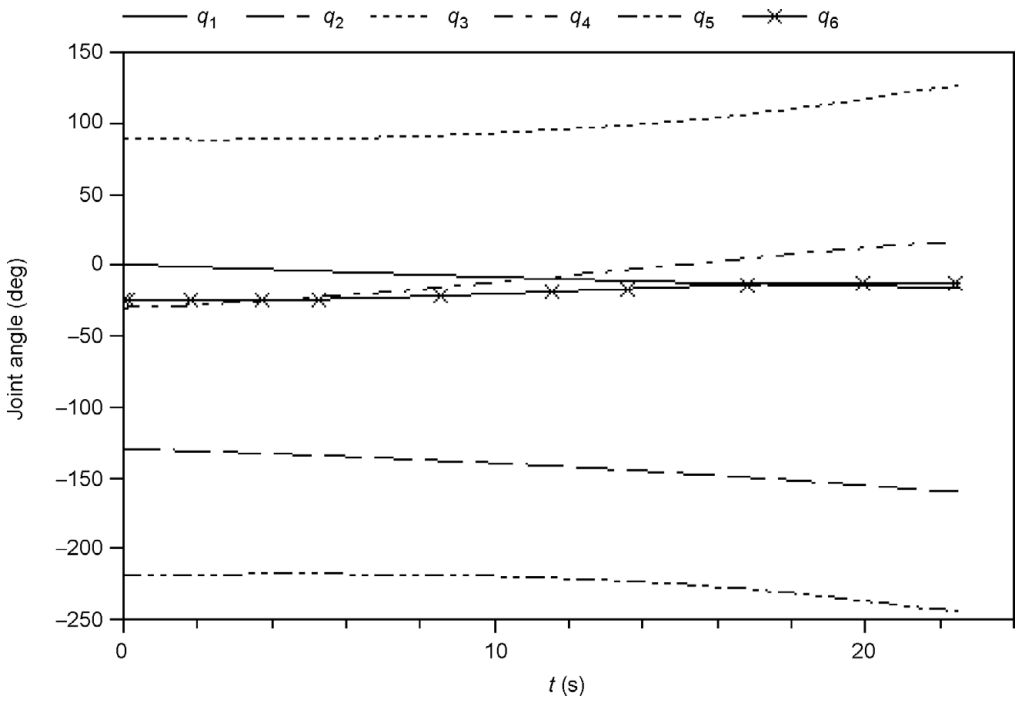

Fig. 10. The joint trajectories of arm-b.

and joint are limited as follows:

$$v_{\max} = 30\,\text{mm/s}, \quad \dot{\theta}_{\max} = 5^\circ/\text{s}. \tag{87}$$

It should be pointed out that Eq. (87) is not a design limit of the space manipulator. It is only the parameter used by motion planning algorithm to limit the maximum values of the planned velocities of the end-effector. These parameters, combined with the Eq. (57), guarantee that the planned joint trajectory is feasible. They are only empirical values for the case considered in this paper and can be modified according to different applications.

Corresponding to the controller structure shown in Fig. 4, the sample time used in the simulation is set as follows:

1. The image processing and pose measurement period of the hand-eye camera is 250 ms (4 Hz).
2. The trajectory generation cycle of the planner is 250 ms (4 Hz).
3. The control cycle of each joint controller is 5 ms (200 Hz). The joint controller autonomous interposes more knots between the current value and the desired value from the planner.

According to the simulation results, the dual-arm space robot autonomously captured the target in coordinated behavior (see Fig. 6) at 22.5 s.

The position of the handles with respect to the end-effectors (measured by the hand-eye cameras mounted on the effectors of arm-a and arm-b) varies as shown in Figs. 7 and 8, respectively. The gradually decreasing close to zero indicates that the end-effectors approach the target into its capture-box and then grasps the target. The trajectory of each joint during the capturing is illuminated as in Figs. 9 and 10, respectively. During the capturing, the base is "free-floating," i.e., its attitude and position are not actually controlled. Therefore,

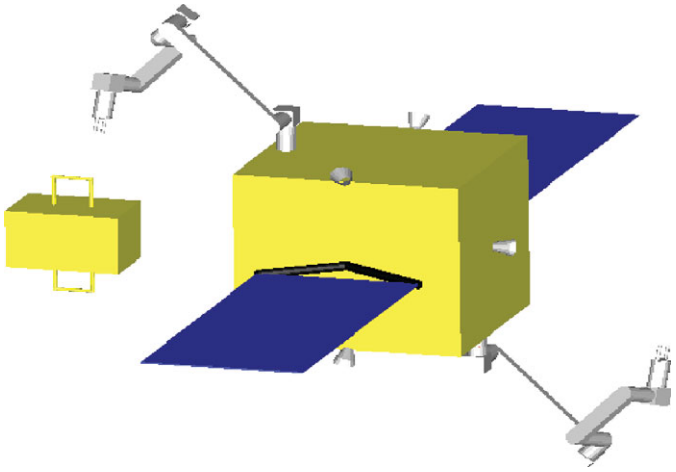

Fig. 11. (Colour online) The initial state.

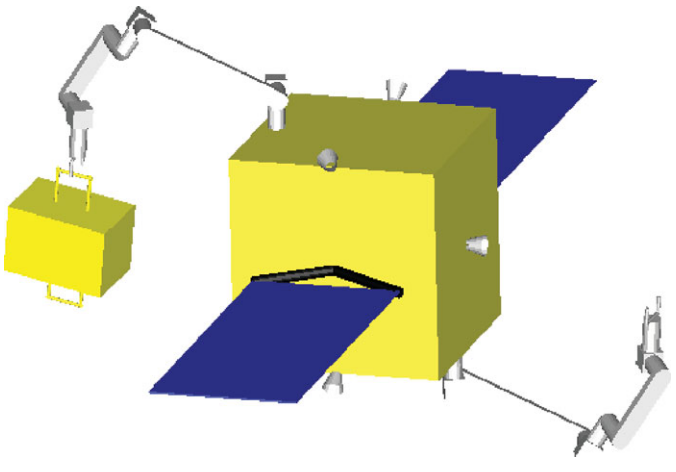

Fig. 12. (Colour online) The final state.

https://doi.org/10.1017/S0263574711001007 Published online by Cambridge University Press

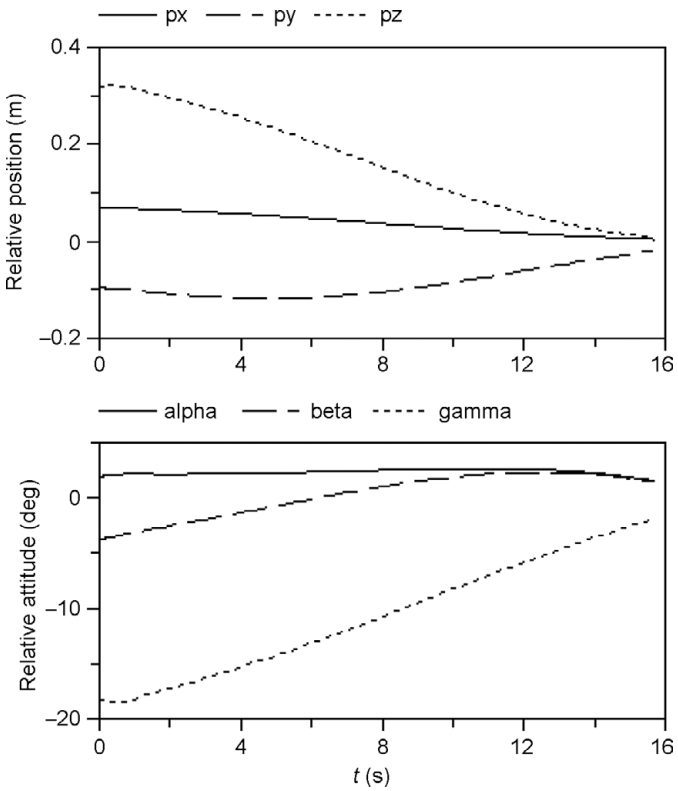

Fig. 13. The variation of the relative pose.

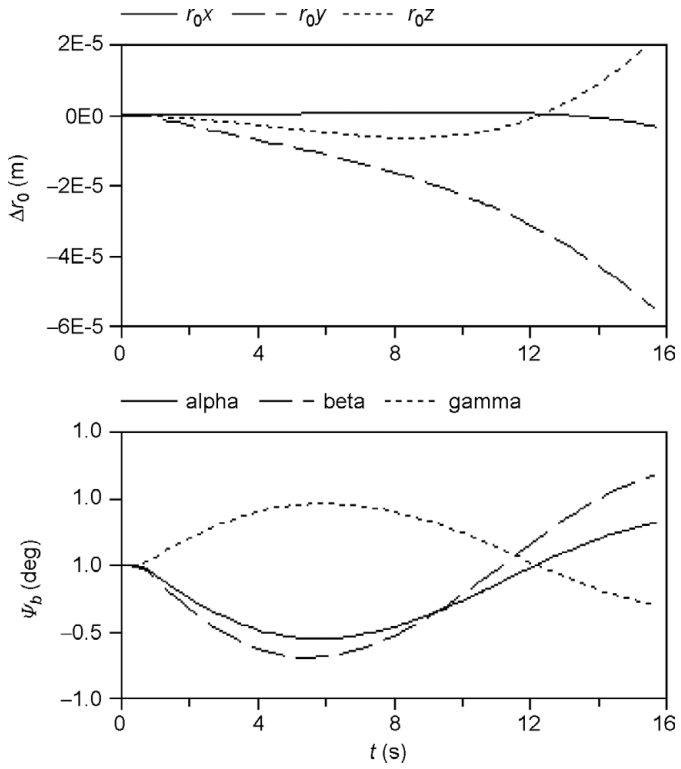

Fig. 14. The variation of the base pose.

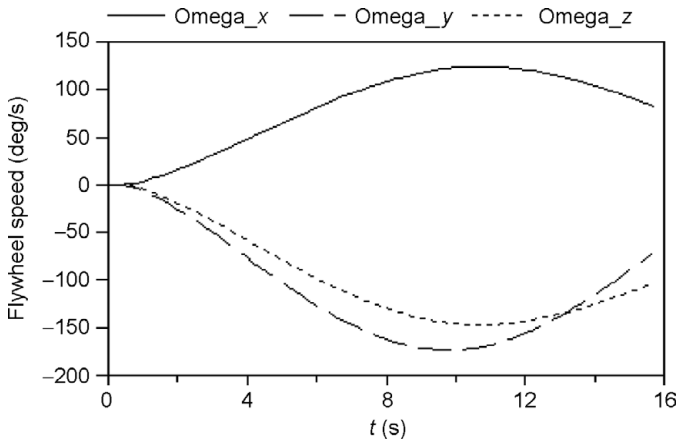

Fig. 15. The motion of the flywheels.

the base moves in response to the reaction of the manipulator. The CM position of the base changes [−0.015 m, −0.028 m, and −0.003 m]^T with respect to its initial position, and the base attitude changes from [0, 0, 0] to [−4.72°, 0.49°, and 1.34°].

4.3. Simulation for the single-arm capturing while keeping the base's inertial pose

For this case, one arm (mission arm, named arm-a) is used to capture the moving target, and the other arm (balance arm, named arm-b) is used to keep the position of the base's CM approximately fixed in the inertial frame. In addition, the attitude of the satellite is stabilized by the reaction wheels. Two arms are designed and mounted centrosymmetrically with respect to the centroid of the base, so that the condition (76) is always satisfied if the two arms move with the same trajectories.

A possible design is shown in Fig. 11, and the vectors to define the two arms' mounted positions are, respectively,

$$\boldsymbol{b}_0^a = \begin{bmatrix} 0.5, & 0, & 0.712 \end{bmatrix}^T, \quad \boldsymbol{b}_0^b = -\begin{bmatrix} 0.5, & 0, & 0.712 \end{bmatrix}^T. \tag{88}$$

The inertia of each reaction flywheel is (the unit is kg.m^2)

$$\boldsymbol{J}_w = 2.86 \times 10^{-2}. \tag{89}$$

In order to clearly illuminate the concept presented in Section 3.3, and compare the results with other cases, the same initial conditions of Section 4.2 are used for simulation, i.e., the initial joint angles of arm-a and arm-b, target position and velocities, and the constraints on the two arms are shown as in Eqs. (81)–(87). According to the simulation results, arm-a autonomously captured the target at 15.7 s. The final state after capturing is shown in Fig. 12. The relative pose varies as in Fig. 13, the monotonous decreasing to zero illuminates that the end-effector approaches the handle until it goes into the capturing-box, i.e., the envelop capability of the end-effector's fingers. During the capturing, both the CM's position and attitude of the base are nearly invariable (the variations of the position and attitude are less than 6e-5 m and 0.75°, respectively, which is shown in Fig. 14). The drive torques of the reaction wheels are between −0.75 Nm and 0.85 Nm, and the angular velocities of the reaction flywheels are shown in Fig. 15. Compared with the case above (Section 4.2), we can see that the space robot captures the target more quickly for the same conditions (only 15.7 s). It is obvious that the inertially fixed base is very useful for quick capturing.

https://doi.org/10.1017/S0263574711001007 Published online by Cambridge University Press

5. Conclusion

Compared with a single-arm space robot, a dual-arm or multi-arm system has much more dexterity and flexibility, and can complete more complex tasks. In this paper, the coordinated motion planning of a dual-arm space robot is studied. Corresponding to different applications, two typical cases are considered. The first case is that two arms are used both to capture the target and manipulate it synchronously. The other case is that one arm is used to capture and manipulate the target, but the other arm is used to keep the base fixed in the inertial frame. Each mode has its own advantages and disadvantages. It is worth mentioning that the method used for the second case supplies an attractive concept, i.e., by elaborate designing and arranging the two arms, the motion of the balance arm can be easily planned to keep the CM position of the base approximately motionless. In order to keep the attitude of the base invariable, the reaction wheel is required to absorb the resultant angular momentums generated by the two arms' motion. If the movement velocities of the space manipulator are relatively large, the generated angular momentum will exceed the capability of the reaction wheel. We are studying the feasibility of designing the structure of a second arm, which is used to compensate the angular and linear momentums simultaneously. Based on the novel design, the trajectory of the balance arm can be easily planned and will not encounter the singularity problem of Eq. (72). In the future, we will set up an air-bearing experiment system and verify the motion planning methods using practical mechanism.

Acknowledgments

This work is supported by National Nature Science Foundation of China (NSFC) under research grant no. 60805033.

References

1. G. Hirzinger, K. Landzettel, B. Brunner, M. Fischer and C. Preusche, "DLR's robotics technologies for on-orbit servicing," *Adv. Robot.* **18**(2), 139–174 (2004).
2. E. Coleshill, L. Oshinowo, R. Rembala, B. Bina, D. Rey and S. Sindelar, "Dextre: Improving maintenance operations on the international space station," *Acta Astronaut.* **64**(9–10), 869–874 (2009).
3. K. Yoshida, "Engineering test satellite VII flight experiments for space robot dynamics and control: Theories on laboratory test beds ten years ago, now in orbit," *Int. J. Robot. Res.* **22**(5), 321–335 (2003).
4. W. F. Xu, B. Liang, C. Li, Y. Liu and Y. S. Xu, "Autonomous rendezvous and robotic capturing of non-cooperative target in spacet," *Robotica* **28**(5), 705–718 (2010).
5. P. Boning and S. Dubowsky, "Coordinated control of space robot teams for the on-orbit construction of large flexible space structures," *Adv. Robot.* **24**(3), 303–323 (2010).
6. S. A. A. Moosavian and E. Papadopoulos, "Free-flying robots in space: An overview of dynamics modeling, planning and control," *Robotica* **25**(5), 537–547 (2007).
7. J. R. Wilson, "Satellite hopes ride on orbital express," *Aerosp. Am.* **45**(2), 30–35 (2007).
8. F. Aghili, "Optimal Control of a Space Manipulator for Detumbling of a Target Satellite," **In**: *Proceedings of IEEE International Conference on Robotics and Automation*, Kobe, Japan (May 12–17, 2009) pp. 3019–3024.
9. I. Rekleitis, E. Martin, G. Rouleau, R. L'Archevêque, K. Parsa and E. Dupuis, "Autonomous capture of a tumbling satellite," *J. Field Robot.* **24**(4), 275–296 (2007) (special issue on Space Robotics).
10. Y. Umetani and K. Yoshida, "Resolved motion rate control of space manipulators with generalized jacobian matrix," *IEEE Trans. Robot. Autom.* **5**(3), 303–314 (1989).
11. Y. Umetani and K. Yoshida, "Workspace and manipulability analysis of space manipulator," *Trans. Soc. Instrum. Control Eng.* **E-1**(1), 116–123 (2001).
12. Richard A. McCourt and C. W. de Silva, "Autonomous robotic capture of a satellite using constrained predictive control," *IEEE/ASME Trans. Mechatronics* **11**(6), 699–708 (2006).
13. E. Papadopoulos and S. Dubowsky, "Coordinated Manipulator/Spacecraft Motion Control for Space Robotic Systems," **In**: *Proceedings of International Conference on Robotics and Autanatim*, Sacramento, CA, USA (April 9–11, 1991) pp. 1696–1701.
14. S. A. A. Moosavian and E. Papadopoulos, "On the kinematics of multiple manipulator space free-flyers and their computation," *J. Robot. Syst.* **15**(4), 207–216 (1998).
15. R. Rastegari and S. A. A. Moosavian, "Multiple impedance control of space free-flying robots via virtual linkages," *Acta Astronaut.* **66**(5–6), 748–759 (2010).
16. Y.-R. Hu and G. Vukovich, "Dynamic control of free-floating coordinated space robots," *J. Robot. Syst.* **15**(4), 217–230 (1998).
17. K. Yoshida, R. Kurazume and Y. Umetani, "Dual Arm Coordination in Space Free-Flying Robot," **In**: *Proceedings of IEEE International Conference on Robotics and Automation* (IEEE Press, Piscataway, NJ, 1991), pp. 2516–2521.
18. K. Yoshida, R. Kurazume and Y. Umetani, "Torque Optimization Control in Space Robots with a Redundant Arm," **In**: *Proceedings of IEEE/RSJ International Workshop on Intelligent Robots and Systems (IROS '91)*, Osaka, Japan (Nov 3–5, 1991) pp. 1647–1652.
19. E. Papadopoulos and S. Dubowsky, "Dynamic singularities in the control of free-floating space manipulators," *ASME, J. Dyn. Syst. Meas. Control* **115**(1), 44–52 (1993).
20. P. F. Huang, Y. S. Xu and B. Liang, "Dynamic balance control of multi-arm free-floating space robots," *Int. J. Adv. Robot. Syst.* **2**(2), 117–124 (2005).
21. S. K. Agrawal and S. Shirumalla, "Planning motions of a dual-arm free-floating manipulator keeping the base inertially fixed," *Mech. Mach. Theory* **30**(1), 59–70 (1995).
22. Y. S. Xu and T. Kanade, *Space Robotics: Dynamics and Control* (Kluwer, Norwell, MA, 1992).
23. Z. Vafa and S. Dubowsky, "The kinematics and dynamics of space manipulators: The virtual manipulator approach," *Int. J. Robot. Res.* **9**(4), 3–21 (1990).
24. Y. Yokokohji, T. Toyoshima and T. Yoshikawa, "Efficient computational algorithms for trajectory control of free-flying space robots with multiple arms," *IEEE Trans. Robot. Autom.* **9**(5), 571–580 (1993).
25. K. Yoshida and Y. Umetani, "Control of Space Manipulators with Generalized Jacobian Matrix," **In**: *Space Robotics: Dynamics and Control* (Y. S. Xu and T. Kanade, eds.) (Kluwer, Norwell, MA, 1993) pp. 165–204.
26. Y. Masutani, F. Miyazaki and S. Arimoto, "Sensory Feedback Control for Space Manipulators," **In**: *Proceedings of IEEE International Conference on Robotics and Automation*, Scottsdale, AZ, USA (May 14–19, 1989) pp. 1346–1351.
27. Y. Masutani, F. Miyazaki and S. Arimoto, "Sensory Feedback Control for Space Manipulators," **In**: *Space Robotics: Dynamics and Control* (Y. S. Xu and T. Kanade, eds.) (Kluwer, Norwell, MA, 1993) pp. 205–227.
28. W. F. Xu, B. Liang and Y. S. Xu, "Practical approaches to handle the singularities of a type of space robotic system," *Acta Astronaut.* **68**(1–2), 269–300 (Jan–Feb 2011).
29. A. Ogilvie, J. Allport, M. Hannah and J. Lymer, "Autonomous Robotic Operations for On-Orbit Satellite Servicing," **In**:

Proceedings of Sensors and Systems for Space Applications II, SPIE, vol. 6958 (R. T. Howard; and P. Motaghedi, eds.) (SPIE, Bellingham WA, 2008), pp. 695809-1–695809-12.

30. P. Motaghedi, "On-Orbit Performance of the Orbital Express Capture System," **In**: *Proceedings of Sensors and Systems for Space Applications II, SPIE*, vol. 6958 (R. T. Howard; and P. Motaghedi, eds.) (SPIE, Bellingham WA, 2008), pp. 69580E-1–69580E-12.
31. R. B. Friend, "Orbital Express Program Summary and Mission Overview," **In**: *Proceedings of SPIE, Sensors and Systems for Space Applications II*, vol. 6958 (R. T. Howard; and P. Motaghedi, eds.) (SPIE, Bellingham WA, 2008), pp. 695803-1–695803-11.

https://doi.org/10.1017/S0263574711001007 Published online by Cambridge University Press